An Evaluation of the GOES-16 Rapid Scan for Nowcasting in Southeastern Brazil: Analysis of a Severe Hailstorm Case

Bruno Z. Ribeiro[1], Luiz A. T. Machado[1], Joao H. Huamán Ch.[1], Thiago S. Biscaro[1]

Edmilson D. Freitas[2], Kathryn W. Mozer[3] and Steven J. Goodman[4]

[1]*Centro de Previsão de Tempo e Estudos Climáticos, Instituto Nacional de Pesquisas Espaciais (CPTEC/INPE), Cachoeira Paulista, São Paulo, Brazil*

[2]*Instituto de Astronomia, Geofísica e Ciências Atmosféricas, Universidade de São Paulo, São Paulo, Brazil*

[3]*NOAA/NESDIS/Office of Satellite and Product Operations, College Park, Maryland*

[4]*GOES-R Program/TGA, Huntsville, Alabama*

*Correspondence to: Bruno Z. Ribeiro, Centro de Previsão de Tempo e Estudos Climáticos /Instituto Nacional de Pesquisas Espaciais (CPTEC/INPE), Rodovia Presidente Dutra, km 39, Cachoeira Paulista - SP, Brasil, 12630-000. E-mail: bruno.ribeiro@inpe.br; URL: *http://www.cptec.inpe.br/*

ABSTRACT: The GOES-16 mesoscale domain sector (MDS) scans with 1 minute intervals are used in this study to analyze a severe thunderstorm case occurred in southeastern Brazil. The main objective is to evaluate the GOES-16 MDS rapid scans against the operational full-disk scans with lower temporal resolution for nowcasting. Data from a C-band radar, observed sounding and a ground-based lightning network are also used in the analysis. A group of thunderstorms formed in the afternoon of 29 November 2017 in an environment of moderate convective available potential energy (CAPE) and deep-layer shear. The storms presented

24 supercell characteristics and intense lightning activity with peak rates in excess of 150 flashes

25 per 5 minutes. The satellite-derived trends with 1-minute interval were skillful in detecting

26 thunderstorm intensification, mainly in the developing stage. The decrease in cloud-top 10.35-

27 μm brightness temperature was accompanied by increases in ice mass flux, concentration of

28 small ice particles at cloud top and storm depth. In the mature stage, there is no evident trend

29 in the satellite-derived parameters that could indicate storm intensification, but the cluster area

30 expands suggesting cloud-top divergence. The 1-minute rapid scans indicate greater lead time

31 to severe weather relative to 10- and 15-minutes resolution imagery, but also presented

32 numerous false alarms (indication of severe weather but no occurrence) due to oscillations in

33 the satellite-derived parameters. The parameters calculated every 5 minutes presented better

34 skill than 10 and 15 minutes and fewer false alarms than 1 minute.

35 *Keywords: severe thunderstorm; hail; rapid scan; GOES; nowcasting; southeastern Brazil*

36

37   **1.   Introduction**

38

39   Nowcasting using satellites entered a new era with the new generation of the National

40 Oceanic and Atmospheric Administration (NOAA) Geostationary Operational Environmental

41 Satellite-R (GOES-R) Series. The GOES-R Series provide geostationary data with

42 unprecedented spatial, temporal and radiometric resolutions over South America with the

43 Advanced Baseline Imager (ABI), as well as lightning data through the Geostationary Lightning

44 Mapper (GLM), and are especially useful for nowcasting in regions with sparse radar coverage

45 (Schmit et al., 2017). Of particular interest for nowcasting purposes is the GOES-R Series ABI

46 mesoscale domain sector (MDS) which provides rapid scanning with a temporal resolution of

47 1 minute or 30 seconds over a movable domain of approximately 1,000 km x 1,000 km that can

2

48 be executed anywhere in the satellite field of view (Schmit et al., 2017). This study focuses on

49 a severe thunderstorm case in Brazil using 1-minute MDS scans.

50   The benefits of satellite scans with high temporal resolution (< 5 minutes interval) for

51 monitoring thunderstorms are explored in several studies (e.g., Dworak et al., 2012; Bedka et

52 al., 2015; Mecikalski et al., 2016; Apke et al., 2016; Line et al., 2016). Severe thunderstorms

53 with strong updrafts can evolve more rapidly than the trends revealed in operational 15-minute

54 full-disk scans (Bedka et al., 2015; Cintineo et al., 2013), so that higher scanning temporal

55 resolution can improve the accuracy of nowcasting techniques, forecaster situational awareness,

56 and increase the lead time (the time between a given parameter trend indicates severe weather

57 is likely and the severe weather is observed at surface) of severe thunderstorm warnings. As an

58 example, Goodman et al. (1988) studied a severe thunderstorm that evolved from no lightning

59 to maximum lightning activity in 7–8 minutes and caused a microburst with small pea-sized

60 hail at the ground four minutes after peak lightning activity. Such rapid storm evolutions are

61 not possible to monitor with scans every 15 minutes (Gatlin and Goodman, 2010).

62   Given that severe thunderstorms can evolve very rapidly, several techniques based on

63 satellite products were developed to identify convective initiation and thunderstorm

64 intensification (e.g., Mecikalski and Bedka, 2006; Mecikalski et al., 2010a; Mecikalski et al.,

65 2010b). Algorithms based on 15-minute resolution are useful for forecasters to identify the

66 thunderstorm characteristics. For example, the updraft trend can be estimated by the rate of

67 decrease of the cloud-top temperature (e.g., Mecikalski et al., 2016) and the cloud-top glaciation

68 can be evaluated by using the tri-spectral difference (e.g., Ackerman et al., 1990; Strabala et

69 al., 1994). The physical properties of the thunderstorms as estimated by satellites can be used

70 to predict the occurrence of severe weather. Even though these algorithms are valuable when

71 using 15-minute satellite data, several studies show that higher temporal resolution can provide

3

72 greater lead time to severe weather when issuing a warning (e.g., Bedka et al., 2015; Bedka et

73 al., 2016). The present study aims at comparing satellite-derived parameters with different

74 temporal resolutions to evaluate the different lead times to severe weather and the advantages

75 of using the MDS scanning for severe subtropical storms over South America.

76   Several studies have used the GOES data to study convection over South America

77 (e.g., Machado et al., 1998; Vila et al., 2008; Durkee and Mote, 2010). Most of these studies

78 focus on the climatological aspects of mesoscale convective systems (Machado et al., 1998;

79 Durkee and Mote, 2010) and extrapolation techniques to forecast convective systems' motion

80 (Vila et al., 2008). Due to the absence of rapid scans over South America, no study has focused

81 on the advantages of using these data in nowcasting in this continent. Even though the use of

82 satellite data is one of the many tools used in severe thunderstorm monitoring, in some regions

83 of South America it is the only spatial data available in real time.

84   During the testing period of the first GOES-R Series satellite (now the operational

85 GOES-16 or GOES East), a 1-minute MDS was made available over southeastern Brazil on 28

86 and 29 November 2018 to support the SOS-CHUVA (System for Observing and Forecasting

87 Severe Weather, acronym in Portuguese; Machado et al., 2014) field campaign intense

88 observation period (IOP). The occurrence of severe storms within the GOES-16 MDS, the

89 ground lightning network and a C-band radar coverage generated an unprecedented opportunity

90 to study severe thunderstorms in Brazil.

91   In this study, the GOES-16 1-minute MDS data are used to analyze two severe

92 hailstorms in southeastern Brazil and evaluate the benefits of rapid scans relative to the formerly

93 available operational scans with 10–30 minutes of frequency. The main scientific questions

94 raised in this study are: What are the main differences between the severe storms that occurred

95 in the region in terms of cloud-top microphysical characteristics as inferred by satellite and

4

96   lightning activity? Do the satellite-derived parameters in severe subtropical storms behave

97   similarly to midlatitude storms previously studied in other regions of the world? Do the 1-

98   minute data provide a significant gain in the nowcasting lead time to severe weather relative to

99   scans with lower temporal resolution for the studied case?

100   This paper is organized as follows: Sec. 2 describes the data and methodology; Sec. 3

101   shows the results, which are divided in the analysis of the pre-convective environment (Sec.

102   3.1), convective initiation and storm evolution (Sec. 3.2), the temporal variations of the

103   satellite-derived parameters and their use in nowcasting (Sec. 3.3) and an evaluation of satellite

104   parameters with different temporal frequencies (Sec. 3.4); The conclusions are presented and

105   discussed in Sec. 4.

106

107   **2.**   **Data and methodology**

108

109   *2.1.*   *The SOS-CHUVA campaign*

110

111   The SOS-CHUVA campaign IOP was held from 27 to 31 November 2017 in

112   southeastern Brazil. During this period, the area of the experiment in southeastern Brazil was

113   sampled by radars, disdrometers, radiosondes, surface stations, hailpads, and the GOES-16 was

114   performing MDS scans with 1-minute intervals over the SOS-CHUVA area and nearby (Fig.

115   1) on 28 and 29 November 2017. The storms in this study were too far from the SOS-CHUVA

116   ground based observation network to utilize that data, but the 29 November 2017 MDS data

117   allowed for an extensive satellite analysis of the storms.

118

119   *2.2*   *GOES-16 data and satellite-derived parameters*

120

121   The GOES-16 ABI (Schmit et al., 2017) channels employed were the 1.6-μm band

122   with 1 km spatial resolution and the bands 6.19 μm, 8.5 μm, 10.35 μm, 11.2 μm and 12.3 μm

123   with 2 km spatial resolution, with all data in the original satellite projection. The satellite was

124   in the post-launch testing period at 89.5°W, west of its operational position (75.2°W). The cloud

125   properties (level-2) had not yet been provisionally validated for operational use, thus only the

126   different ABI channels were used in this study.

127   A clustering method was applied to the GOES-16 data to identify convective systems

128   and calculate the Lagrangian satellite-derived parameters. The method is based on the

129   ForTraCC (Vila et al., 2008), in which a cluster is defined as a continuous area of at least 40

130   pixels with 10.35-μm brightness temperature (Tb) lower than 235 K. By using the tracking

131   algorithm, it was possible to compute the cloud cluster size and temporal evolution (Machado

132   and Laurent, 2004), and the cloud top Tb in different channels (Mecikalski et al. 2010a;

133   Mecikalski et al. 2010b). Table 1 shows a summary of each satellite-derived parameter with the

134   respective critical values used for monitoring deep convection. In this study, we used the

135   minimum or maximum value of the parameter in the cluster to evaluate the temporal trends,

136   since extreme values are generally related to the strongest convective updrafts. The parameters

137   were calculated with intervals of 1, 5, 10 and 15 minutes.

138   One of the main variables used to estimate the convective cloud depth is the 10.35-

139   μm Tb. Lower Tb relates to deeper cloud tops simply because the temperature decreases with

140   height in the troposphere (Adler and Mack, 1986). The updraft strength can be estimated by the

141   temporal derivative of the 10.35-μm Tb (Adler and Fenn, 1979; Roberts and Rutledge, 2003;

142   Mecikalski and Bedka, 2006). In general, cloud-top cooling rates greater than 4 K in 15 minutes

143   indicate a convective updraft, while cooling rates of 8 K in 15 minutes are associated with a

6

144   vigorous updraft (Mecikalski and Bedka, 2006). The difference between 6.19- and 10.35-μm

145   Tb also provides estimates of the cloud depth. Negative values are associated with clear regions

146   or shallow clouds, while in cases of deep convection, when the cloud tops reach the tropopause

147   or lower stratosphere, the 6.19–10.35-μm difference is positive (Fritz and Laszlo, 1993;

148   Ackerman 1996; Schmetz et al. 1997; Mecikalski and Bedka, 2006; Machado et al. 2009).

149   The cloud-top particle size is estimated using the 1.6-μm band reflectance, which

150   associate lower reflectance values with larger particle size and vice-versa (Baum et al., 2000).

151   An increase in the 1.6-μm band reflectance for cloud-top temperatures above 233 K is also

152   linked to glaciation. The reflectance values of this band were obtained by converting the

153   reflectance factor to reflectance using $1/\cos(\theta)$, where θ is the solar zenith angle. In this case,

154   due to the fact that reflectance values become undefined with solar zenith angles near 90°

155   (Lindsey et al., 2006), only times before 1950 UTC were considered in this study, when the

156   zenith angle is nearly 72° in this location. The difference between 8.5 μm and 11.2 μm is used

157   to monitor cloud-top ice crystal sizes as well. This difference is positive in cloud tops containing

158   ice crystals. High positive values are associated with smaller ice crystals and low positive values

159   with larger ice crystals (Ackerman et al. 1990).

160   Cloud-top glaciation and variations in ice mass flux are inferred by using the tri-

161   spectral difference (Ackerman et al. 1990; Strabala et al. 1994), which is based on the different

162   values of water and ice absorption coefficients in the 8.5–12.3-μm range. Positive values of the

163   tri-spectral difference $[(8.5 - 11.2 \, \mu\text{m}) - (11.2 - 12.3 \, \mu\text{m})]$ can be attributed to ice crystals and

164   negative values to water droplets.

165

166   *2.3.   Other datasets*

167

7

168   Data from the C-band radar located in Mateus Leme (19.94°S, 43.43°W, 1270 m

169   altitude; Fig. 1b) were also used. The radar has a beam width of 1 degree, radial resolution of

170   250 m, wavelength of 5.328 cm, and generates a volume scan with 10 elevations every 5

171   minutes. This radar is operated by the *Companhia Energética de Minas Gerais* (CEMIG).

172   Unfortunately, polarimetric variables and radial winds data were very noisy in the studied

173   period, thus only the reflectivity is used in this study. The two storms were tracked using the

174   0.5° plan position indicator (PPI) horizontal reflectivity factor with the reflectivity threshold of

175   40 dBZ to define a storm cluster. The centroid of the reflectivity core is used as a proxy for the

176   storm location, which allowed for tracking the position of the storm every 5 minutes (frequency

177   of radar scans), generating a radar-derived trajectory for each storm. The maximum reflectivity

178   and average vertically-integrated liquid (VIL) are also calculated every 5 minutes for each

179   storm cluster.

180   The lightning data used in this study derives from the BrasilDAT network, which

181   encompasses more than 70 lightning sensors (Earth Networks). The BrasilDAT detection

182   efficiency is greater than 90% (for both intra-cloud and cloud-to-groung lightning flashes) over

183   southeastern Brazil (Naccarato and Pinto, 2009). The total lightning (sum of cloud-to-ground

184   and cloud-to-cloud lightnings) was used in this study because this quantity is physically related

185   to storm/updraft intensity and provides greater skill in nowcasting than the use of cloud-to-

186   ground lightning alone (e.g., Schultz et al., 2009; Wu et al., 2018). The lightning strikes

187   occurred within 10 km from the pixel with minimum 10.35-μm Tb of the cluster in each 1-

188   minute interval were manually associated with each storm, and lightning density refers to the

189   number of strikes associated with the storm accumulated in 5-minute intervals. Since the GLM

190   sensor was being tested during this period, we decided to use only BrasilDAT data.

191   The convective environment was accessed using the Global Forecast System [GFS,

192   from the National Centers for Environmental Prediction (NCEP)] model analysis. The GFS is

193   a T1534 global model with 64 vertical levels starting a new integration every 6 h. The model

194   output is interpolated to a 0.25° resolution grid, which is used in this study. Sounding data of

195   the Confins Airport (SBCF; 19.62°S, 43.67°W; Fig. 1) were taken from the University of

196   Wyoming website (http://weather.uwyo.edu/).

197

198   **3.   Results**

199

200   On the afternoon of 29 November 2017, severe storms occurred in east-central Minas

201   Gerais state (Fig. 1) and caused severe winds and large hail (Fig. 2). In the city of Caeté, hail

202   of nearly 5 cm in diameter was responsible for widespread damage to buildings and vehicles

203   (Fig. 2a). According to the local Civil Defense, 14 people were injured, more than 300 had to

204   leave their homes and 2,050 buildings were damaged. The cities of Ribeirão das Neves and

205   Pedro Leopoldo, located approximately 100 and 120 km, respectively, to the northwest of Caeté

206   (Fig. 1b), were affected by other storm nearly two hours after Caeté (Fig. 2b). Pedro Leopoldo

207   reported 5-cm hail, whereas severe winds and 2-cm hail occurred in Ribeirão das Neves,

208   producing damage to roofs and trees on both cities. The storms in the region occurred between

209   1630 and 2100 UTC. No severe weather reports were associated with the other storms in the

210   region on this day. This study focuses only on the two storms that were confirmed as severe.

211

212   *3.1 Pre-convective environment*

213

214   Figure 3 shows the GFS analysis fields at 1800 UTC 29 November 2017, when

215   convective activity was increasing in the region. A broad cyclonic circulation is observed over

9

216   the Atlantic Ocean with attendant cyclonic vorticity maximum near the coast of Brazil (Fig.

217   3a). Minas Gerais state is in the northwestern periphery of the cyclonic circulation, where

218   southwesterly flow predominates. There is no cyclonic vorticity maximum upstream of the

219   region. A 500-hPa temperature trough is over the affected cities at this time with 500-hPa

220   temperatures of nearly −9°C. Relatively cold air in the midtroposphere is known to favor hail

221   growth (e.g., Johnson and Sugden, 2014). The strongest 500-hPa winds (>15 m s^{-1}) occur along

222   the Brazilian coast, where the upper-level jet is located (not shown).

223   The 850-hPa level 1800 UTC fields are shown in Fig. 3b. A surface cold front moved

224   northeastwards over the Atlantic Ocean on 28 November (one day before; not shown) and

225   stalled along the higher terrain in the coast of Brazil (Fig. 1). Lower 850-hPa equivalent

226   potential temperature (θe) is found over the Atlantic Ocean in association with southeasterly

227   flow, which causes enhanced 1000–700-hPa moisture flux convergence (MFC) along the

228   Brazilian coast. MFC is also observed along a ridge oriented in the south-southwest to north-

229   northeast direction in central Minas Gerais (Fig. 1b), where the three affected cities are located

230   and the 850-hPa θe is higher. The MFC along this ridge occurs due to the east-southeasterly

231   winds at low-levels and serves as a focus for convective initiation after 1600 UTC. These

232   synoptic fields provide evidence that the storms formed under weak synoptic-scale forcing for

233   ascent.

234   The 1200 UTC 29 November 2017 sounding at SBCF (Fig. 4) depicts a relatively

235   moist air mass between surface and ~600 hPa. The sounding site is no more than 50 km from

236   the area where the storms occurred. A mixed layer is observed in the first kilometer above

237   surface indicating the boundary layer mixing due to radiative heating in the beginning of the

238   day (1200 UTC is 0900 local time). Steep temperature lapse rates and lower relative humidity

239   are observed above the 600-hPa level. Even though the most unstable CAPE is only 200 J kg^{-1}

10

240   at this time, this temperature/dewpoint temperature profile can attain higher instability during

241   the afternoon in response to low-level radiative heating, which corroborates CAPE values of

242   1189 J kg^{-1} in SBCF at 1800 UTC according to the GFS analysis. The equilibrium level for

243   surface-based parcels is at nearly 180 hPa, where the temperature is approximately −60°C (213

244   K). Also, the easterly low-level winds turn to southwesterly midlevel winds and cause 0–6-km

245   wind shear of more than 20 m s^{-1}, which is sufficient for severe storms with rotating updrafts

246   (e.g., Thompson et al., 2003).

247

248   *3.2   Convective initiation and storm evolution*

249

250   The estimated time of hailfall in Caeté (Fig. 1b) is 1740 UTC and in Pedro Leopoldo

251   is 1930 UTC. Ribeirão das Neves was affected at nearly 1900 UTC by the same storm that hit

252   Pedro Leopoldo. The hail occurrence time was estimated based on reports of local officials,

253   videos in social media and radar imagery, and there is an associated error in the estimate of +−

254   5 minutes. Therefore, we use a 10-minute period centered in the most probable time of hailfall

255   to account for this error. This study focuses on the two severe thunderstorms that produced 5-

256   cm hail in Caeté and Pedro Leopoldo, which are referred as Caeté storm (CTS) and Pedro

257   Leopoldo storm (PLS).

258   Figure 5 shows the evolution of the 10.35-μm Tb from 1630 to 2015 UTC every 15

259   minutes. The first time the CTS reached Tb colder than 235 K is at 1645 UTC (Fig. 5b), which

260   is followed by an increase in the area colder than 235 K in the next 45 minutes (Figs. 5c,d). The

261   coldest Tb of the entire CTS life time (212 K from the 1-minute data at 1736 UTC; Figure 5e)

262   is attained after the system intensification at 1730 UTC (Fig. 5e), nearly 10 minutes before

263   hailfall. The minimum Tb of CTS is relatively high compared to severe storms documented in

264   the literature (e.g., Bedka et al., 2012; Bedka et al., 2015; Bedka et al., 2018). Also, there is no

265   V- or U-shape signature (e.g., Setvák et al., 2010; Setvák et al., 2013) discernible at the CTS

266   top, but an east-northeastward propagation of the anvil related to high winds aloft. At 1745

267   UTC (Fig. 5f), the minimum Tb in CTS cluster is over the city of Caeté. After this time (Figs.

268   5g–j), CTS weakens and dissipates at nearly 1900 UTC (Fig. 5k). No severe thunderstorm

269   signature is observed in the satellite imagery [V-shape, overshooting top or above-anvil cirrus

270   cloud (Bedka et al., 2018)] besides the cloud-top cooling.

271   The PLS forms at nearly 1800 UTC (Fig. 5g) 100 km west-southwest of CTS. This

272   storm presents a distinct Tb minimum at 1845 and 1900 UTC (Figs. 5j,k), when 2-cm hail and

273   damaging winds were registered in Ribeirão das Neves. A V-shape signature, also indicative of

274   a vigorous updraft, is discernible at 1915 UTC (Fig. 5l), nearly 15 minutes before the 5-cm

275   hailfall at Pedro Leopoldo. Noticeably, the PLS has minimum Tb of 203 K at 1946 UTC, nearly

276   9 K lower than CTS, which indicates a deeper updraft in PLS storm as compared to CTS. The

277   lower minimum Tb in PLS cluster is possibly associated with the greater thermodynamic

278   instability (CAPE) in the northern part of the study area and/or rotating, more undiluted updrafts

279   in this storm. Other storms that formed near PLS also had minimum Tb lower than storms that

280   formed in the south of the study region or earlier, such as CTS (not shown). The PLS cluster

281   merges with the other cluster farther south at nearly 1935 UTC.

282   Imagery every 1 minute allowed the identification of multiple "pulses" of convective

283   intensification and momentary Tb decrease. A similar behavior was observed in other severe

284   storms (e.g., Apke et al., 2018). Witt et al. (2018), for example, studied the supercell that

285   generated the El Reno, OK, EF3 tornado on 31 May 2013 and noticed multiple updrafts during

286   a quasi-steady phase of the storm occurred after a period of rapid intensification. The storm was

287   distinguished as a classic supercell after the last of these pulses.

12

288   Figure 6 shows CTS and PLS radar-derived trajectories along with total lightning

289   between 1600 and 2100 UTC, and the clusters areas with Tb lower than 235 K at the estimated

290   time of hail reports (1740 and 1930 UTC, respectively). The radar-derived trajectories and

291   lightning paths clearly show slow storm motion during the first 40 minutes of the storms

292   lifetimes, followed by a leftward turn and acceleration of storm motion. The 0–6-km mean wind

293   derived from the 1800 UTC sounding is shown in Fig. 6 as evidence that the storms were

294   initially advected by the mean wind but then changed the direction of motion, moving to the

295   left of the mean wind. This behavior is a well-known and extensively documented signature of

296   supercells, long-lived storms with a rotating updraft, since the perturbation pressure gradient

297   associated with the convective core causes a deflection of the storm motion from the mean wind

298   (Rotunno and Klemp, 1982). The individual trajectories of other storms in the region (not

299   shown) followed the 0–6-km mean wind to the east-northeast whereas the supercells moved

300   north-northeastward.

301   The horizontal reflectivity factor PPIs and vertical cross sections (Fig. 7) also support

302   that the storms were supercells. Hook echoes are observed in low elevation scans at 1730 UTC

303   in CTS (Fig. 7a) and at 1930 UTC in PLS (Fig. 7d). Hook echoes curved to the north are

304   characteristic of cyclonic supercells (left movers) in the Southern Hemisphere (Nascimento et

305   al., 2014), where the warm/moist storm-relative inflow is from the north. The hook echo

306   signature is distinct in several radar scans of CTS and PLS (not shown). Hail cores with

307   reflectivity greater than 60 dBZ are observed at heights above the 0°C isotherm (Figs. 7b,e).

308   Additionally, vertical cross sections nearly through the hook echoes (Figs. 7c,f) evidence the

309   bounded weak echo region (BWER; e.g., Marwitz, 1972) associated with the absence of large

310   hydrometeors within the intense updraft, which is also characteristic of supercells.

311   The CTS caused more lightning strikes than the PLS in the first hour after initiation

312   (Fig. 6). Both storms present an increase in lightning activity before hailfall, which matches the

313   leftward turn of the radar-derived trajectories. This rapid increase in lightning activity that is

314   observed before severe weather occurs is referred to as a lightning jump (Goodman et al., 1988).

315   This pattern also suggests the lightning activity increased when the mesocyclones intensified,

316   since the deviant motion became more pronounced. CTS dissipates nearly one hour after the

317   hail occurrence, but the PLS intensifies after causing hail. CTS dissipation occurs in nearly the

318   same period of PLS intensification. It is possible that the gust front from the CTS intensifies

319   the PLS updraft as reported by Goodman and Knupp (1993) and others, or the compensatory

320   subsidence from PLS causes CTS weakening.

321

322   *3.3   Temporal evolution of the satellite-derived parameters*

323

324   In this section, the 1-minute satellite-derived parameters and the lightning density are

325   analyzed. The objective is to evaluate what parameters show better indications of severe

326   weather in the temporal trends and what is the lead time.

327   Figure 8 shows the temporal trends in the satellite-derived parameters. The CTS 10.35-

328   μm Tb (Fig. 8a) varies around the value of 225 K before 1705 UTC, when it drops to a minimum

329   of 216 K. This decrease in Tb is observed in the Tb temporal trend (Fig. 8b) as a minimum

330   cooling rate of -3 K min^{-1}. This moment is when the first deep updraft of CTS occurs (Fig. 5d).

331   After this abrupt decrease, Tb remains steady between 215 and 220 K. Another intense updraft

332   occurs after 1728 UTC and causes a Tb decrease of nearly 12 K in 7 minutes, which is

333   equivalent to an average cooling of 1.71 K min^{-1} or 25.65 K in 15 minutes, more than three

334   times greater than the 8 K cooling in 15 minutes threshold of Mecikalski and Bedka (2006) for

335   a vigorous updraft. The decrease in minimum 10.35-μm Tb after 1728 UTC (Fig. 8a) and the

14

336   minimum Tb temporal trend occurred at 1730 UTC (Fig. 8b) precedes the most probable time

337   of hailfall by nearly 10 minutes. These trends are accompanied by an increase in lightning

338   activity from 19 lightning flashes between 1725 and 1730 UTC to 46 flashes in the next 5

339   minutes (lightning jump), which precedes the severe event nearly 10–15 minutes, in agreement

340   with other studies (e.g., Williams et al., 1999; Gatlin and Goodman, 2010; Schultz et al., 2011).

341   The updraft observed after 1728 UTC is responsible for an increase in the tri-spectral

342   difference (Fig. 8c), which changes from negative before 1728 UTC to positive after this time,

343   and attains nearly 4°C between 1730 and 1735 UTC. This behavior occurs in response to the

344   increase in cloud-top ice crystals as the updraft penetrates the upper troposphere (Ackerman et

345   al. 1990). The increase in the concentration of small ice particles at the cloud top is the

346   explanation for the increase in albedo (Fig. 8e) as well, since small ice particles reflect more

347   solar radiation in the 1.6-μm band than large ice particles. The 8.5–11.2-μm Tb difference (Fig.

348   8f) behaves very similarly to the other variables, with an increase in the difference preceding

349   the hail event and in phase with the lightning activity. This increase is associated with an

350   increasing amount of ice crystals in the top of the convective cloud.

351   The 6.19–10.35-μm difference (Fig. 8d) also increases with the time, but the temporal

352   trend is more continuous and only shows the cloud top height is increasing. The stratosphere

353   was at nearly 120 hPa according to the 1200 UTC observed sounding (Fig. 4) and the minimum

354   tropopause temperature was –77°C (196 K), while the minimum Tb of CTS was 212 K (–61°C),

355   which indicates this storm did not penetrate into the stratosphere. The 6.19–10.35-μm difference

356   does not describe the short-time storm variability associated to the updraft intensification,

357   which agrees with the behavior found by Yost et al. (2017). The area and area expansion (now

358   shown) have a same behavior, i.e, capture the intensification but show no short-term variability.

359   Apke et al. (2018) also concluded that the trends in upper-level divergence (which can be

15

360   roughly related to the anvil area expansion) are not useful in describing short-term storm

361   intensification, in particular for supercell storms that present cyclic behavior.

362   Figure 9 presents the same parameters of Fig. 8, but for the PLS. A clear lightning

363   jump is observed prior to the first severe event (2-cm hail and wind damage in Ribeirão das

364   Neves) at nearly 1900 UTC. There is a decrease in 10.35-μm Tb (Fig. 9a) in the same period,

365   as well as an increase in the tri-spectral (Fig. 9c) and 8.5–11.2-μm differences (Fig. 9f) and an

366   increase in the 1.6-μm albedo (Fig. 9e), all of them indicating an intensification of the

367   convective updraft.

368   The period before the second severe event caused by PLS (5-cm hail in Pedro

369   Leopoldo) was remarkably different from the periods before the other severe events in terms of

370   lightning activity. A decrease in lightning density occurs after 1900 UTC, and the lightning

371   density remains stable around 20 flashes per 5 minutes until 1930 UTC. The lightning density

372   then increases rapidly *at nearly the same time* the severe hail occurred in Pedro Leopoldo, not

373   before it as commonly observed. The lightning density increases to more than 150 flashes per

374   5 minutes after the severe event, which is one order of magnitude greater than before. This

375   period of high lightning density of PLS will be analyzed later in this section.

376   The 10.35-μm Tb decreases between 1916 and 1920 UTC in association with a subtle

377   lightning density increase between 1915 and 1920 UTC. In the same period, the other

378   parameters show a *decrease*, even though the tendencies are expected be positive in areas of

379   convective invigoration. On the other hand, the values of the satellite-parameters are high

380   compared to the CTS (Fig. 8) and the period preceding the first severe weather event of PLS.

381   For example, the tri-spectral difference (Fig. 9c) varies between 3°C and 8°C before and during

382   the second severe weather event of PLS in Pedro Leopoldo, while it peaks at 4°C before the

383   CTS event. We hypothesize the PLS enters in the mature stage after the first severe weather

16

384 event, when the 10.35-μm Tb is lower than 210 K. Both the tri-spectral difference (Fig. 9c) and

385 the 8.5–11.2-μm difference (Fig. 9f) indicate there is an increase in ice mass flux and in the

386 concentration of small ice particles at the cloud top, which are associated with an active updraft.

387 The 6.19–10.35-μm difference (Fig. 9d) denotes a slow increase in cloud depth with time, but

388 no jump before the severe event as observed for CTS (Fig. 8d).

389   The evolution of the reflectivity profile and VIL derived from the C-band radar for

390 CTS and PLS is shown in Fig. 10. The updrafts as inferred by the decreases in 10.35-μm Tb are

391 consistent with reflectivity increases above the freezing level and at the top of the storm, mainly

392 for the CTS (Fig. 10a). There is an increase in reflectivity below and near the 0°C isotherm and

393 in VIL before hailfall in both cases, but for the PLS (Fig. 10b) there is a noticeable decrease in

394 reflectivity and VIL associated with the hailfalls, which is consistent with the decrease in

395 hydrometeors within the storm as precipitation occurs.

396   The maturation of PLS after 1910 UTC is supported by the 10.35-μm Tb, which

397 becomes lower than 210 K. This value is nearly the temperature of the equilibrium level as

398 indicated by the 1200 UTC observed sounding (Fig. 4), which indicates the PLS updraft

399 probably reached the tropopause (Bedka and Khlopenkov, 2016). When the updraft reaches the

400 tropopause and encounters the stable air in this layer, the primary growth occurs in the

401 horizontal, and it can be seen as an anvil area expansion (Mecikalski et al., 2016). Fig. 11

402 evidences that the area increases to almost 2000 km² 20–30 minutes before the first PLS severe

403 weather event, decreases after 1852 UTC, and then increases more rapidly after 1900 UTC.

404 This last rapid increase in the PLS cluster area denotes the horizontal expansion of the anvil as

405 the updraft reaches the tropopause (Machado and Laurent, 2004; Mecikalski et al., 2016; Apke

406 et al., 2018). At 1932 UTC, the PLS cluster merges with another cluster and the area expansion

407 is not monitored anymore. No severe weather reports were found in this period, but the lightning

17

408   trends suggest that the PLS intensified even further after the 5-cm hailfall in Pedro Leopoldo at

409   nearly 1930 UTC.

410   The satellite-derived parameters and lightning density during the mature stage of PLS

411   are shown in Fig. 12. The lightning density increase is evident after 1930 UTC, when the

412   lightning density increases from nearly 30 to more than 150 lightning flashes per 5 minutes in

413   a period of roughly 30 minutes. The radar reflectivity signature (not shown) depicts a prominent

414   hook echo at this time, which is a signature of updraft rotation and presence of a mesocyclone

415   in the thunderstorm. It is possible that the mesocyclone played a role on the maintenance of the

416   PLS by inducing greater thunderstorm organization and limiting the disruption of the updraft

417   by the downdraft (e.g., Houze, 2004).

418   The 10.35-μm Tb (Fig. 12a) varies between 202 and 209 K in the period, which is

419   slightly lower than the estimated temperature of the equilibrium layer (210 K). Some updrafts

420   are more intense and cause momentary 10.35-μm Tb decrease, such as between 1940 and 1945

421   UTC and 2012 and 2017 UTC, but there is no total trend in 10.35-μm Tb in the period. The tri-

422   spectral difference (Fig. 12c) and 8.5–11.2-μm Tb difference (Fig. 12b) indicate increasing ice

423   mass flux. The difference between 6.9-μm Tb and 10.35-μm Tb (Fig. 12d) is steady at nearly –

424   2 °C, which indicates the thunderstorm depth remains constant during the period and reinforces

425   the idea that the updrafts are not able to reach the stratosphere (overshoot) at this moment. As

426   the storm expands and attains the mature stage, the variability of the parameters decreases, and

427   the 1-minute scans do not produce additional information of the storm for nowcasting purposes.

428   Even though both storms produced large hail, there were significant differences

429   between the two severe storms. The satellite-derived parameters and lightning activity suggest

430   the CTS storm intensified, produced large hail, and dissipated, while PLS lightning activity

431   increased further after the large hail and maturation. The CTS was shallower and did not present

18

432 characteristic overshooting top or V-shape, while the PLS was deeper and had severe signatures

433 in satellite imagery. Despite these differences, the 1-minute trends proved to be useful

434 indicators of the severe hailfalls. This study is the first to contrast two storms that occurred in

435 the same environment, produced similar severe weather impacts, but had different satellite

436 signatures, and to highlight the forecasting potential of the 1-minute satellite-derived

437 parameters trends even for such different storms.

438

439   *3.4*   *Comparison of satellite parameters in different temporal resolutions*

440

441   Figure 13 shows the satellite-derived parameters with different temporal resolutions

442 for the CTS cluster. The 1-minute trends show much more variability and details than the other

443 temporal resolutions. The 10.35-μm Tb decrease from 1728 to 1736 UTC (Fig. 13a), which

444 precedes the hail event, is not captured by the 10- and 15-minute resolutions. The minimum

445 10.35-μm Tb of the entire CTS lifetime (212 K at 1736 UTC) is missed in the 10 and 15-minute

446 resolutions as well. The 5-minute resolution data, however, is able to represent both the Tb drop

447 and the Tb minimum with good similarity to the 1-minute data. The lead time of the 10.35-μm

448 Tb (i.e., decrease in Tb preceding the hail occurrence) is similar when using data with 1 and 5

449 minutes, but is much lower using data with 10 or 15 minute resolutions. The decrease in Tb and

450 the association of it with the intensification of the CTS updraft would be noted only at the time

451 of the event for the 10- and 15-minute resolutions, and the updraft intensity estimated by Tb

452 trends is lower (Mecikalski et al., 2016).

453   The other satellite-derived parameters preceding the CTS hail event (Figs. 13b,c,d)

454 show a similar pattern. The 5-minute curves follow the 1-minute curves closely, even though

455 they are not able to capture the 1-minute pulses. For the 1.6-μm albedo (Fig. 13b) the maximum

19

456   that precedes the CTS event occurs at 1732 UTC (close to 1730 UTC, when both 5-, 10- and

457   15-minute resolutions have a measurement), and the trends are also observed in the 5-, 10- and

458   15-minute data. However, the increase in albedo would be noticed at these resolutions only *at*

459   *the time* of maximum 1.6-μm albedo (1730 UTC), while the increase in albedo with 1-minute

460   data would be noticed 3 minutes before. The 8.5–11.2-μm differences and the tri-spectral

461   difference present two maxima at nearly 1713 and 1734 UTC and a minimum between them at

462   1725 UTC. These variations are again better described by the 1- and 5-minute data, which

463   allows for better monitoring of the increases and decreases in storm intensity. The 15-minute

464   curve for the 8.5–11.2-μm difference (Fig. 13c), for example, is not able to depict the minimum

465   at nearly 1725 UTC, and consequently the positive tendency after this time. The 6.19–10.35-

466   μm difference, area and area expansion were not shown because the 1-minute image and 15

467   minutes images are similar and, at least for these events, these parameters do not introduce new

468   information at higher temporal resolutions.

469   The same graphics are shown for the PLS in Fig. 14. The tendencies lead to similar

470   conclusions in comparison to the CTS case: the 5-minute data is able to follow the 1-minute

471   data in most of the peaks. Even though the 10- and 15-minute data present a 10.35-μm Tb

472   decrease with time (Fig. 14a), there is no discernible rapid decrease that could be associated

473   with an updraft intensification before the first severe event from PLS, precluding the issuance

474   of a warning. After 1910 UTC, when the PLS enters the mature stage, the trends are less useful

475   for predicting the severe weather occurrences, and the advantages of the 1- and 5-minute data

476   are less evident. However, other signatures such as area expansion and the presence of U- or

477   V-shape, can be used by a forecaster to evaluate the storm's severity.

478   The MDS 1-minute data as compared to the more conventional scanning resolutions

479   of 5, 10 and 15 minutes shows details that the other resolutions are not able to capture.

20

480   Variations in cloud-top properties and updraft intensity occurring in a few minutes are only

481   measured by the rapid scan. The lead times of 1-minute trends were nearly 12 minutes for the

482   CTS event and 8 and 12 minutes for the first and second PLS events, respectively, which is

483   lower than the lead times found by Bedka et al. (2015) for storms in the U.S. For nowcasting

484   purposes, the 5-minute scans can describe the main tendencies of the satellite-derived

485   parameters and also filter the 1-minute trends that may not be associated directly with a trend

486   in storm intensity. A warning system based on the 1-minute data without any temporal filter

487   could cause too many false alarms. An example appears in the trends of the tri-spectral

488   difference for the PLS (Fig. 14d) between 1905 and 1940 UTC, in which the 1-minute data

489   shows several maxima and minima within an oscillatory pattern while the 5-minute data

490   presents a smoothed curve indicating a more stable behavior of the parameter. The 1-minute

491   trends in this case could lead to false alarms. A possible explanation for the results using 5-

492   minute data is the fact that most updrafts accompanied by Tb decrease occur in the range

493   between 5 and 10 minutes, which allows at least one measurement of the Tb drop with 5-

494   minutes interval. Bedka and Khlopenkov (2016) developed an algorithm for overshooting top

495   detection that incorporates parameters such as visible channel texture, which improve the

496   association of 1-minute trends with severe weather reports by reducing false alarms. Also, the

497   indication of severe weather by the 10- and 15-minutes trends is better before the first PLS

498   event (Fig. 14) than before the CTS event (Fig. 13), which suggests there is a case-to-case

499   variability in the skill of each scan frequency. This analysis relies on only two cases and a

500   statistical analysis with a high number of cases is deserved.

501

502   **4.   Conclusions**

503

21

504   Two storms responsible for severe hail and wind reports in southeastern Brazil were

505   analyzed using the GOES-16 MDS scans. Lagrangian satellite-derived quantities commonly

506   used in nowcasting were calculated for these storms by using a cluster tracking algorithm. The

507   analysis benefited from data of a C-band radar and a lightning detection network in the same

508   region.

509   The storm responsible for 5-cm hail in Caeté presented severe signatures in radar but

510   not in the satellite imagery. The minimum cloud-top 10.35-μm Tb was 212 K, which is higher

511   than the minimum of other storms nearby. The satellite-derived parameters indicate the CTS

512   probably did not reach the equilibrium level at the tropopause, which relates to its relatively

513   warm cloud top. Between 10 and 15 minutes before the occurrence of hail caused by the CTS,

514   the satellite-derived parameters showed a rapid decrease in 10.35-μm Tb (peaking at −3 K per

515   minute), which is much more intense than the decrease rates found by Mecikalski and Bedka

516   (2006) using satellite data with 15 minutes of temporal resolution, and a lightning jump. The

517   other parameters also indicated increasing concentration of small ice particles at the cloud top

518   and increasing ice mass flux. The 6.19–10.35-μm difference shows an increase in value, but

519   does not show any signature of penetrative cloud and does not show the short-time variability,

520   but a nearly continuous monotonic increase in the cloud depth. The 6.19–10.35-μm difference

521   did not attain positive values, which corroborates that an overshooting top was not observed in

522   the CTS. The CTS weakens after the severe weather event and dissipates at nearly 1900 UTC.

523   The PLS also presented supercell characteristics and produced two severe weather

524   events at different times. For the first severe weather event, the parameters indicated a rapid

525   decrease in cloud-top temperature, increase in ice mass flux and increase in storm depth 10-15

526   minutes before the event, plus a lightning jump. The second event occurred during the transition

527   of PLS to the mature stage, when the satellite-derived parameters stabilize and subsequently

22

528   the lightning density increases. There are no clear tendencies in the satellite-derived parameters

529   that could indicate updraft invigoration, but only the maintenance of an intense updraft.

530   However, radar signatures and the occurrence of V-shape during some moments after

531   maturation (not shown) and high lightning activity suggest the storm was still severe at this

532   time. It is also possible that severe weather occurred between the first and the second PLS

533   events, but no reports were found.

534   The PLS evolved to the mature stage after 1940 UTC, with lightning densities over

535   150 lightning flashes per 5 minutes in some moments and a relative stability of the satellite

536   derived parameters, along with 10.35-μm near and below the equilibrium level temperature. It

537   is possible that the deeper updraft and greater increase in ice mass flux of the PLS are associated

538   with a sustained mesocyclone that maintained the storm organization for more time than the

539   CTS. The area where the PLS formed and the time of the day (late afternoon) suggest the CAPE

540   was higher than when the CTS formed, which could have contributed to a deeper storm. In

541   general, the satellite and radar observations indicate the studied storms had similar

542   characteristics of severe storms in other parts of the world (e.g., Bedka et al., 2015; Mecikalski

543   et al., 2016; Yost et al., 2018).

544   The advantages of the rapid scan in nowcasting are clear when comparing the 1-minute

545   data with the operational 15-minute data. There are several rapid oscillations in the storm

546   intensity, such as updraft intensity, cloud-top glaciation/increase in ice mass flux and storm

547   depth changes, that are only perceivable using the 1-minute data. This is in agreement with

548   Mecikalski et al. (2016), which showed the 1-minute 10.35-μm Tb has good correlation with

549   the amount of CAPE in the layer where the updraft is occurring. One of the main findings of

550   this study is that the 5-minute data showed good representation of the storm-scale oscillations

551   in this case. Also, the 5-minute data is able to smooth the oscillations shown in the 1-minute

23

552   data and can facilitate the nowcasting process by reducing the false alarm to severe weather. A

553   meteorologist monitoring the 1-minute parameters trend would see several positive and

554   negative trends that are not associated with severe weather. The benefit of 1-minute scans is

555   very high relative to 10- or 15-minute scans, but is not significant against 5-minute scans in the

556   present methodology. However, the use of additional information, such as visible channel

557   texture, can reduce the 1-minute false alarms in automated algorithms (Bedka and Khlopenkov,

558   2016). Another advantage of the 1-minute trends is the indication of increasing severe weather

559   potential even for storms that do not have a distinct severe signature (e.g., overshooting top, V-

560   shape), which allows the forecaster to issue a warning when these signatures are absent.

561   The 1-minute trends in the satellite-derived parameters proved to be an important tool

562   for nowcasting and much better at describing storm intensity fluctuations than the operational

563   15- and 10-minute scans mainly for the convective initiation and maturation periods. The study

564   suggests the investigation of other cases to understand this change of time variability as the

565   storm evolve during the life cycle. The ability of 5-minute scans to describe the most important

566   trends in storm intensity can be used to plan operational procedures in satellite scans in the

567   future. Scans of the GOES full disk at 5-minute intervals, for example, can help improve

568   nowcasting over a large area, while the rapid scans only focus on a small domain. Also,

569   upcoming research using the MDS rapidscans over South America during the RELAMPAGO

570   field campaign may provide additional conclusions regarding the use of rapidscans in

571   nowcasting.

572

24

581

582   **References**

583

584   Adler, R. F., and Fenn, D. D., 1979: Thunderstorm vertical velocities estimated from

585   satellite data. Journal of the Atmospheric Sciences, 36(9), 1747-1754.

586   Adler, R. F., and Mack, R. A., 1986: Thunderstorm cloud top dynamics as inferred

587   from satellite observations and a cloud top parcel model. Journal of the atmospheric sciences,

588   43(18), 1945-1960.

589   Ackerman, S. A., Smith, W. L., Revercomb, H. E., and Spinhirne, J. D., 1990: The

590   27–28 October 1986 FIRE IFO Cirrus Case Study: Spectral Properties of Cirrus Clouds in the

591   8–12 μm Window. Monthly Weather Review. https://doi.org/10.1175/1520-

592   0493(1990)118<2377:TOFICC>2.0.CO;2.

593   Ackerman, S. A., 1996: Global satellite observations of negative brightness

594   temperature differences between 11 and 6.7 μm. Journal of the atmospheric sciences, 53(19),

595   2803-2812.

596   Apke, J. M., Mecikalski, J. R., and Jewett, C. P., 2016: Analysis of mesoscale

597   atmospheric flows above mature deep convection using super rapid scan geostationary satellite

598   data. *Journal of Applied Meteorology and Climatology*, *55*(9), 1859-1887.

599   Apke, J. M., Mecikalski, J. R., Bedka, K., McCaul Jr, E. W., Homeyer, C. R., & Jewett,

600   C. P., 2018: Relationships between Deep Convection Updraft Characteristics and Satellite-

601   Based Super Rapid Scan Mesoscale Atmospheric Motion Vector–Derived Flow. *Monthly*

602   *Weather Review*, *146*(10), 3461-3480.

603   Baum, B. A., Soulen, P. F., Strabala, K. I., King, M. D., Ackerman, S. A., Menzel, W.

604   P., and Yang, P., 2000: Remote sensing of cloud properties using MODIS airborne simulator

605   imagery during SUCCESS: 2. Cloud thermodynamic phase. Journal of Geophysical Research:

606   Atmospheres, 105(D9), 11781–11792.

607   Bedka, K. M., Dworak, R., Brunner, J., and Feltz, W., 2012: Validation of satellite-

608   based objective overshooting cloud-top detection methods using CloudSat cloud profiling radar

609   observations. *Journal of Applied Meteorology and Climatology*, *51*(10), 1811-1822.

610   Bedka, K. M., Wang, C., Rogers, R., Carey, L. D., Feltz, W., and Kanak, J., 2015:

611   Examining deep convective cloud evolution using total lightning, WSR-88D, and GOES-14

612   super rapid scan datasets. *Weather and Forecasting*, *30*(3), 571-590.

613   Bedka, K. M., & Khlopenkov, K., 2016: A probabilistic multispectral pattern

614   recognition method for detection of overshooting cloud tops using passive satellite imager

615   observations. *Journal of Applied Meteorology and Climatology*, *55*(9), 1983-2005.

616   Bedka, K., Murillo, E. M., Homeyer, C. R., Scarino, B., and Mersiovsky, H., 2018:

617   The Above-Anvil Cirrus Plume: An Important Severe Weather Indicator in Visible and Infrared

618   Satellite Imagery. *Weather and Forecasting*, *33*(5), 1159-1181.

619   Cintineo, J. L., Pavolonis, M. J., Sieglaff, J. M., and Heidinger, A. K., 2013: Evolution

620   of severe and nonsevere convection inferred from GOES-derived cloud properties. *Journal of*

621   *Applied Meteorology and Climatology*, *52*(9), 2009-2023.

622   Durkee, J. D., and Mote, T. L., 2010: A climatology of warm- season mesoscale

623   convective complexes in subtropical South America. *International Journal of Climatology*,

26

624   *30*(3), 418-431.

625   Dworak, R., Bedka, K., Brunner, J., and Feltz, W., 2012: Comparison between GOES-

626   12 overshooting-top detections, WSR-88D radar reflectivity, and severe storm reports. *Weather*

627   *and Forecasting*, *27*(3), 684-699.

628   Fritz, S., and Laszlo, I., 1993: Detection of water vapor in the stratosphere over very

629   high clouds in the tropics. Journal of Geophysical Research: Atmospheres, 98(D12), 22959-

630   22967.

631   Gatlin, P. N., and Goodman, S. J., 2010: A total lightning trending algorithm to identify

632   severe thunderstorms. *Journal of atmospheric and oceanic technology*, *27*(1), 3-22.

633   Goodman, S. J., Buechler, D. E., Wright, P. D., and Rust, W. D., 1988: Lightning and

634   precipitation history of a microburst- producing storm. *Geophysical research letters*, *15*(11),

635   1185-1188.

636   Goodman, S. J., and K.R. Knupp, 1993: Tornadogenesis via squall line and supercell

637   interaction: The November 15, 1989 Huntsville, Alabama tornado, The Tornado: Its Structure,

638   Dynamics, Prediction, and Hazards, AGU Geophys. Monogr. Series, 79, 183-199.

639   Hersbach, H., 2016: The ERA5 Atmospheric Reanalysis. *AGU Fall Meeting, San*

640   *Francisco, CA, AGU Fall Meeting Abstracts*.

641   Houze, R. A., 2004: Mesoscale convective systems. *Reviews of Geophysics*, *42*(4).

642   Johnson, A. W. and K. E. Sugden, 2014: Evaluation of sounding-derived

643   thermodynamic and wind-related parameters associated with large hail events. Electronic J.

644   Severe Storms Meteor., 9 (5), 1–42.

645   Lindsey, D. T., Hillger, D. W., Grasso, L., Knaff, J. A., & Dostalek, J. F., 2006: GOES

646   Climatology and Analysis of Thunderstorms with Enhanced 3.9-μm Reflectivity. *Monthly*

647   *Weather Review*, 134(9), 2342-2353.

27

648   Line, W. E., Schmit, T. J., Lindsey, D. T., and Goodman, S. J., 2016: Use of

649   geostationary super rapid scan satellite imagery by the Storm Prediction Center. *Weather and*

650   *Forecasting*, *31*(2), 483-494.

651   Machado, L. A. T., Rossow, W. B., Guedes, R. L., and Walker, A. W., 1998: Life

652   cycle variations of mesoscale convective systems over the Americas. *Monthly Weather Review*,

653   *126*(6), 1630-1654.

654   Machado, L. A. T., and Laurent, H., 2004: The convective system area expansion over

655   Amazonia and its relationships with convective system life duration and high-level wind

656   divergence. Monthly weather review, 132(3), 714-725.

657   Machado, L. A., Lima, W. F., Pinto Jr, O., and Morales, C. A., 2009: Relationship

658   between cloud-to-ground discharge and penetrative clouds: A multi-channel satellite

659   application. Atmospheric Research, 93(1-3), 304-309.

660   Machado, L. A., Silva Dias, M. A., Morales, C., Fisch, G., Vila, D., Albrecht, R., ...

661   and Cohen, J., 2014: The CHUVA project: How does convection vary across Brazil?. *Bulletin*

662   *of the American Meteorological Society*, *95*(9), 1365-1380.

663   Marwitz, J. D., 1972: The structure and motion of severe hailstorms. Part III: Severely

664   sheared storms. *Journal of Applied Meteorology*, *11*(1), 189-201.

665   Mecikalski, J. R., and Bedka, K. M., 2006: Forecasting convective initiation by

666   monitoring the evolution of moving cumulus in daytime GOES imagery. *Monthly Weather*

667   *Review*, *134*(1), 49-78.

668   Mecikalski, J. R., MacKenzie Jr, W. M., Koenig, M., and Muller, S., 2010a: Cloud-

669   top properties of growing cumulus prior to convective initiation as measured by Meteosat

670   Second Generation. Part I: Infrared fields. Journal of Applied Meteorology and Climatology,

671   49(3), 521-534.

672   Mecikalski, J. R., MacKenzie Jr, W. M., König, M., and Muller, S., 2010b: Cloud-top

673   properties of growing cumulus prior to convective initiation as measured by Meteosat Second

674   Generation. Part II: Use of visible reflectance. Journal of Applied Meteorology and

675   Climatology, 49(12), 2544-2558.

676   Mecikalski, J. R., Jewett, C. P., Apke, J. M., and Carey, L. D., 2016: Analysis of

677   cumulus cloud updrafts as observed with 1-min resolution Super Rapid Scan GOES imagery.

678   *Monthly Weather Review*, *144*(2), 811-830.

679   Naccarato, K. P., and Pinto Jr, O., 2009: Improvements in the detection efficiency

680   model for the Brazilian lightning detection network (BrasilDAT). *Atmospheric Research*, *91*(2–

681   4), 546–563.

682   Nascimento, E. L., Held, G., and Gomes, A. M., 2014: A Multiple-Vortex Tornado in

683   Southeastern Brazil. *Monthly Weather Review*, *142*(9), 3017-3037.

684   Rotunno, R., and Klemp, J. B., 1982: The influence of the shear-induced pressure

685   gradient on thunderstorm motion. *Monthly Weather Review*, *110*(2), 136-151.

686   Roberts, R. D., and Rutledge, S., 2003: Nowcasting storm initiation and growth using

687   GOES-8 and WSR-88D data. *Weather and Forecasting*, *18*(4), 562-584.

688   Schmetz, J., Tjemkes, S. A., Gube, M., and Van de Berg, L., 1997: Monitoring deep

689   convection and convective overshooting with METEOSAT. Advances in Space Research,

690   19(3), 433-441.

691   Schmit, T. J., Goodman, S. J., Gunshor, M. M., Sieglaff, J., Heidinger, A. K.,

692   Bachmeier, A. S., ... and Rudlosky, S., 2015: Rapid Refresh information of significant events:

693   Preparing users for the next generation of geostationary operational satellites. *Bulletin of the

694   American Meteorological Society*, *96*(4), 561-576.

695   Schmit, T. J., Griffith, P., Gunshor, M. M., Daniels, J. M., Goodman, S. J., and Lebair,

696 W. J., 2017: A closer look at the ABI on the GOES-R series. *Bulletin of the American*

697 *Meteorological Society*, *98*(4), 681-698.

698 Schultz, C. J., Petersen, W. A., and Carey, L. D., 2009: Preliminary development and

699 evaluation of lightning jump algorithms for the real-time detection of severe weather. *Journal*

700 *of Applied Meteorology and Climatology*, *48*(12), 2543-2563.

701 Schultz, C. J., Petersen, W. A., and Carey, L. D., 2011: Lightning and severe weather:

702 A comparison between total and cloud-to-ground lightning trends. *Wea. Forecasting*, **26**, 744–

703 755, doi:10.1175/WAF-D-10-05026.1.

704 Setvák, M., Lindsey, D. T., Novák, P., Wang, P. K., Radová, M., Kerkmann, J., ... and

705 Charvát, Z., 2010: Satellite-observed cold-ring-shaped features atop deep convective clouds.

706 *Atmospheric Research*, *97*(1-2), 80-96.

707 Setvák, M., Bedka, K., Lindsey, D. T., Sokol, A., Charvát, Z., Šťástka, J., &and Wang,

708 P. K., 2013: A-Train observations of deep convective storm tops. *Atmospheric research*, *123*,

709 229-248.

710 Strabala, K. I., Ackerman, S. A., and Menzel, W. P., 1994: Cloud properties inferred

711 from 8–12-µm data. Journal of Applied Meteorology, 33(2), 212-229.

712 Thompson, R. L., Edwards, R., Hart, J. A., Elmore, K. L., and Markowski, P., 2003:

713 Close proximity soundings within supercell environments obtained from the Rapid Update

714 Cycle. *Weather and Forecasting*, *18*(6), 1243-1261.

715 Vila, D. A., Machado, L. A. T., Laurent, H., and Velasco, I., 2008: Forecast and

716 Tracking the Evolution of Cloud Clusters (ForTraCC) using satellite infrared imagery:

717 Methodology and validation. *Weather and Forecasting*, *23*(2), 233-245.

718 Williams, E. R., B. Boldi, A. Matlin, M. Weber, S. Hodanish, D. Sharp, S. Goodman,

719 R. Raghavan, and D. Buechler, 1999: The Behavior of Total Lightning Activity in Severe

720   Florida Thunderstorms, Special Issue of Atmospheric Research, 51, 245-265.

721   Witt, A., Burgess, D. W., Seimon, A., Allen, J. T., Snyder, J. C., and Bluestein, H. B.,

722   2018: Rapid-scan Radar Observations of an Oklahoma Tornadic Hailstorm producing Giant

723   Hail. *Weather and Forecasting*, (2018).

724   Wu, F., Cui, X., and Zhang, D. L., 2018: A lightning-based nowcast-warning approach

725   for short-duration rainfall events: Development and testing over Beijing during the warm

726   seasons of 2006–2007. *Atmospheric Research*, *205*, 2-17.

727   Yost, C. R., Bedka, K. M., Minnis, P., Nguyen, L., Strapp, J. W., Palikonda, R.,

728   Khlopenkov, K., Spangenberg, D., Smith, W. L. Jr., Protat, A., and Delanoë, J., 2018: A

729   prototype method for diagnosing high ice water content probability using satellite imager data.

730   *Atmospheric Measurement Techniques*, *11*(3), 1615-1637.

731

732

733　　　　　　　　　　　　　Table 1: Interest fields and critical values.

Physical attribute	Interest field	Critical values
Particle size	1.6-μm reflectance	Low values → large particles size High values → small particles size
	8.5-μm Tb – 11.2-μm Tb	High positive values → large ice crystals Low negative values → large ice crystals
Cloud-top glaciation/ice mass flux	(8.5-μm Tb – 11.2-μm Tb) – (11.2-μm Tb – 12.3-μm Tb)	> 0 → ice crystals < 0 → water droplets
Cloud depth	6.19-μm Tb – 10.35-μm Tb	> –10 K → deep cloud
	10.35-μm Tb	Tb < 273 K→ deep cloud
Updraft strength	Temporal derivative of 10.35-μm Tb	$dTb/dt < -4$ K (15 min)$^{-1}$ → updraft $dTb/dt < -8$ K (15 min)$^{-1}$→ vigorous updraft

734

32

758   magnitude.

759   FIG. 5: GOES-16 10.35-μm Tb (K) at (a) 1630, (b) 1645, (c) 1700, (d) 1715, (e) 1730,

760   (f) 1745, (g) 1800, (h) 1815, (i) 1830, (j) 1845, (k) 1900, (l) 1915, (m) 1930, (n) 1945, (o) 2000

761   and (p) 2015 UTC. The CTS cluster, PLS cluster, and other noteworthy features are indicated

762   in the figures, as well as the occurrences of hail in each estimated time. All images were

763   displaced to account for the parallax error.

764   FIG. 6: GOES-16 10.35-μm Tb (K, shaded) in the CTS and PLS clusters (Tb<235 K)

765   at 1740 and 1930 UTC, respectively, BrasilDAT total flashes (magenta dots, accumulated in 5-

766   minute intervals according to the colorbar) and CTS and PLS trajectories derived from the 0.5°

767   plan position indicator reflectivity centroids at each 5 minutes. The Caeté, Ribeirão das Neves

768   and Pedro Leopoldo counties areas are delimited by thin black contours, and the stars mark the

769   location of hail reports. The small squares along the storms trajectories indicate the time every

770   5 minutes, and the larger squares the time every 40 minutes (UTC, numbers at the left of the

771   squares). The satellite-derived clusters were displaced to account for the parallax error.

772   FIG. 7: Mateus Leme C-band radar reflectivity factor (dBZ) plots for CTS and PLS.

773   CTS (a) 1.4° and (b) 5.0° PPIs and (c) vertical cross section along the 90° azimuth between A

774   and B at 1730 UTC 29 November 2017. PLS (d) 2.3° and (e) 7.0° PPIs and (f) vertical cross

775   section along the 49° azimuth between C and D at 1930 UTC 29 November 2017. Hook echoes,

776   hail cores and BWERs are indicated.

777   FIG. 8: Temporal variation of (a) minimum 10.35-μm Tb (K, red line), (b) temporal

778   trend of 10.35-μm Tb (K min^{-1}, black line), (c) maximum tri-spectral difference (K, green line),

779   (d) maximum difference between 6.19-μm Tb and 10.35-μm Tb (K, magenta line), (e)

780   maximum 1.6-μm albedo (yellow line) and (f) maximum difference between 8.5-μm Tb and

781   11.2-μm Tb (K, dark red line) for the CTS cluster using GOES-16 data every 1 minute. The

34

782   blue dashed line is the lightning strikes density (right vertical axis). The lightning density value

783   is centered in the middle of the 5-minute period of accumulation. The shaded area is the

784   estimated time of hailfall in Caeté. In the X axis, the colored labels are minutes relative to

785   hailfall and black labels are time (UTC). The main physical processes associated with the trends

786   are described. The grey line below the X axis indicates the periods when a hook echo was

787   evident on radar in low elevation scans and/or a BWER was evident in cross sections.

788   FIG. 9: Same as Figure 8, but for the PLS cluster. The leftmost shaded area is the

789   Ribeirão das Neves 2-cm hail and wind event and the rightmost shaded area is the Pedro

790   Leopoldo 5-cm hail event. In the X axis, the colored labels are minutes relative to hailfall (for

791   each event according to the color) and black labels are time (UTC). The main physical processes

792   associated with the trends are described. The grey line below the X axis indicates the periods

793   when a hook echo was evident on radar in low elevation scans and/or a BWER was evident in

794   cross sections.

795   FIG. 10: Temporal evolution of the vertical profile of reflectivity (dBZ, shaded) and

796   average VIL (mm, white line) for the (a) CTS and (b) PLS clusters. The estimated times of

797   hailfall are shown between grey lines. The light blue line indicates the 0°C isotherm height

798   estimated using the 1200 UTC sounding (Fig. 4). The updrafts as inferred by the 10.35-μm Tb

799   decreases (Fig. 8a for CTS and Fig. 9a for PLS) are indicated by black arrows.

800   FIG. 11: Temporal variation of the PLS cluster area (km²). The leftmost shaded area

801   is the Ribeirão das Neves 2-cm hail and wind event and the rightmost shaded area is the Pedro

802   Leopoldo 5-cm hail event. In the X axis, the colored labels are minutes relative to hailfall (for

803   each event according to the color) and black labels are time (UTC).

804   FIG. 12: Temporal variation of (a) minimum 10.35-μm Tb (K, red line), (b) maximum

805   difference between 8.5-μm Tb and 11.2-μm Tb (K, dark red line), (c) maximum tri-spectral

806 difference (K, green line) and (d) maximum difference between 6.19-μm Tb and 10.35-μm Tb

807 (K, magenta line) for the PLS cluster mature stage using GOES-16 data every 1 minute. The

808 blue dashed line is the lightning strikes density (right vertical axis). The lightning density value

809 is centered in the middle of the 5-minute period of accumulation. The shaded area is the

810 estimated time of hailfall in Pedro Leopoldo.

811   FIG. 13: Temporal variations of the satellite-derived parameters each 1 (blue dotted

812 line), 5 (magenta dot-dashed line), 10 (orange dashed line) and 15 (green continuous line)

813 minutes for the CTS cluster. (a) Minimum 10.35-μm Tb (K), (b) maximum 1.6-μm albedo, (c)

814 maximum difference between 8.5-μm Tb and 11.2-μm Tb (K) and (d) maximum tri-spectral

815 difference (K). The shaded area is the estimated time of hailfall in Caeté. In the X axis, the

816 colored labels are minutes relative to hailfall and black labels are time (UTC). The occurrences

817 of vigorous updrafts [8 K (15 min)$^{-1}$ decrease in 10.35-μm Tb] noticed in 1- and 5-minute scans

818 but not in 10- and 15-minute scans are indicated.

819   FIG. 14: Temporal variations of the satellite-derived parameters each 1 (blue dotted

820 line), 5 (magenta dot-dashed line), 10 (orange dashed line) and 15 (green continuous line)

821 minute for the PLS cluster. (a) Minimum 10.35-μm Tb (K), (b) maximum difference between

822 6.9-μm Tb and 10.35-μm Tb (K), (c) maximum difference between 8.5-μm Tb and 11.2-μm Tb

823 (K) and (d) maximum tri-spectral difference (K). The leftmost shaded area is the Ribeirão das

824 Neves 2-cm hail and wind event and the rightmost shaded area is the Pedro Leopoldo 5-cm hail

825 event. In the X axis, the colored labels are minutes relative to hailfall (for each event according

826 to the color) and black labels are time (UTC). The occurrences of vigorous updrafts [8 K (15

827 min)$^{-1}$ decrease in 10.35-μm Tb] noticed in 1- and 5-minute scans but not in 10- and 15-minute
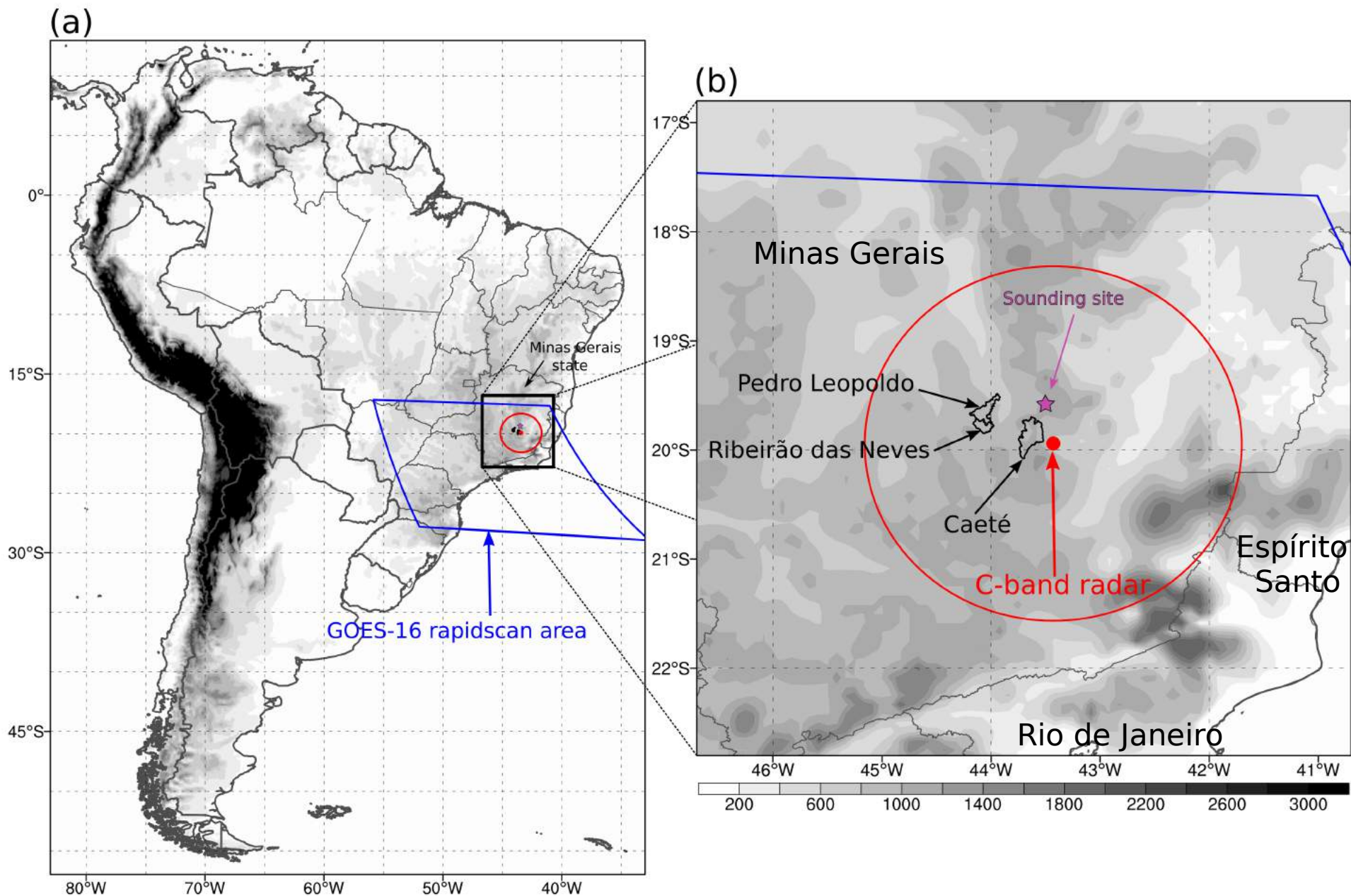
828 scans are indicated.

829

36

FIG. 1: Map showing the study region in the Minas Gerais state, southeastern Brazil, and the areas of the affected counties (Caeté, Ribeirão das Neves and Pedro Leopoldo). The GOES-16 rapid scan area during 29 November 2017 is delimited by the blue polygon. The red dot is the location of Mateus Leme C-band radar (19.94°S, 43.43°W, 1270 m altitude) and the red circle is the area covered by the radar (250-km radius). The magenta star is the location of the SBCF sounding site. The state of Minas Gerais in southeastern Brazil is also indicated.

FIG. 2: Photos of the hailstones and associated damage on 29 November 2017. (a) 4–5-cm hailstones in Caeté and (b) hail accumulation in a street of Pedro Leopoldo.
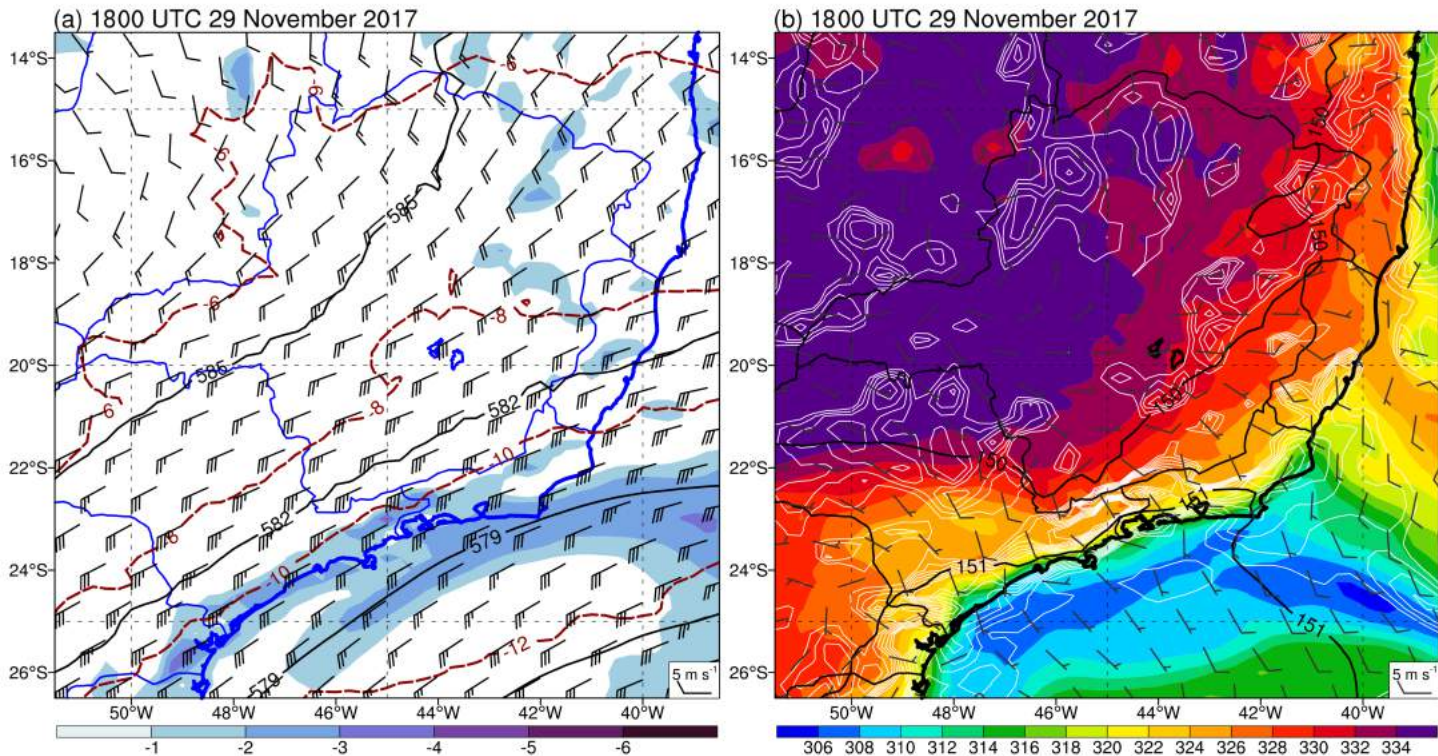
FIG. 3: GFS analysis at 1800 UTC 29 November 2017. (a) 500-hPa relative vorticity (10^{-5} s^{-1}, shaded), temperature (°C, red dashed contours), geopotential height (dam, black continuous contours) and winds (m s^{-1}, pennant is 25 m s^{-1}, full barb is 5 m s^{-1}, and half barb is 2.5 m s^{-1}). (b) 850-hPa θe (K, shaded), geopotential height (dam, black contours) and winds (m s^{-1}, pennant is 25 m s^{-1}, full barb is 5 m s^{-1}, and half barb is 2.5 m s^{-1}), and 1000–700-hPa MFC (10^{-5} g kg^{-1} s^{-1}, white contours every 3 x 10^{-5} g kg^{-1} s^{-1} starting at 3 x 10^{-5} g kg^{-1} s^{-1}). Contours of the counties affected by severe weather are drawn.
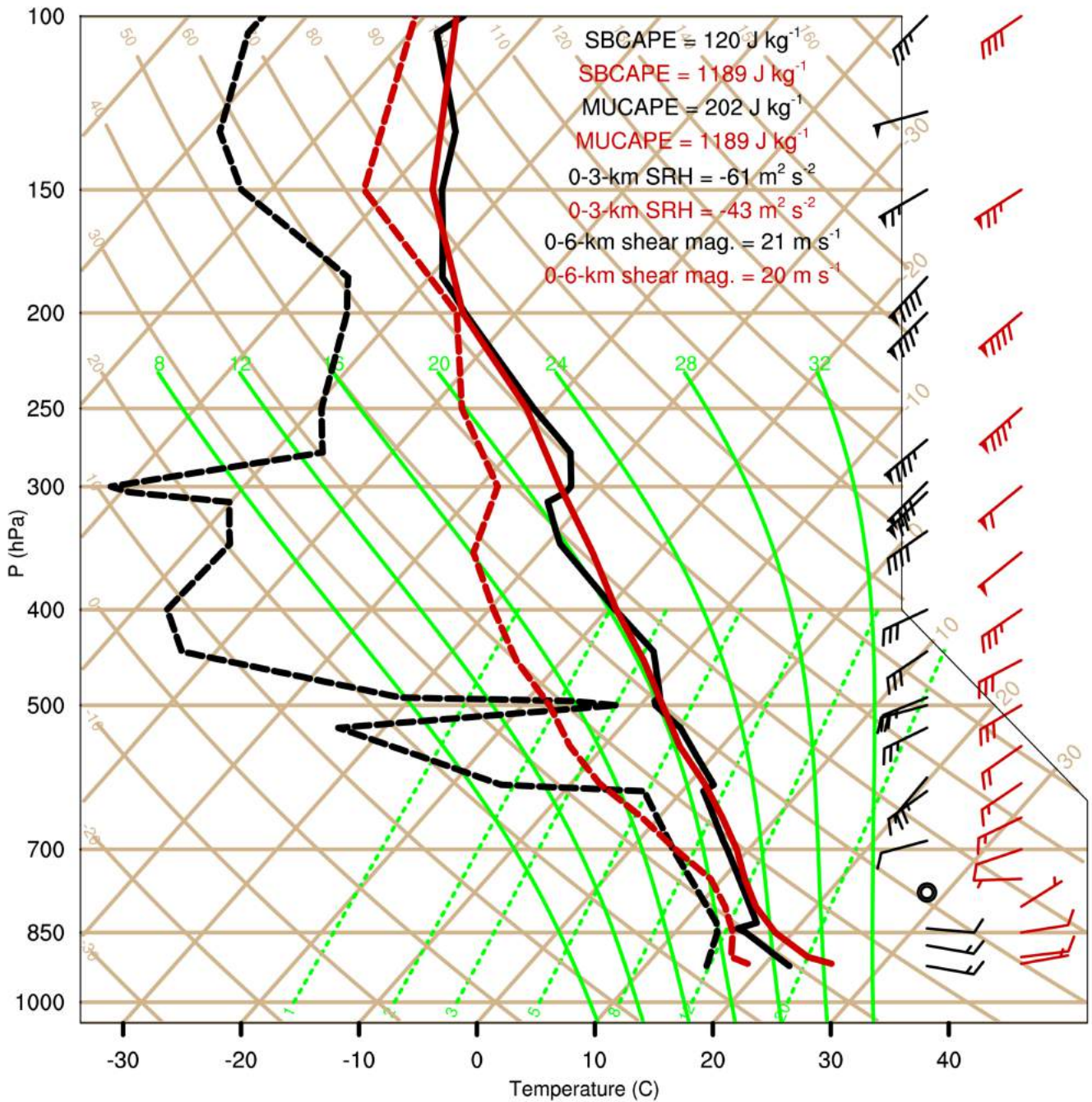
FIG. 4: Skew T/log p diagram showing the 29 November 2017 soundings at Confins Airport (19.62°S, 43.67°W; Fig. 1) where the continuous line indicates the temperature and the dashed line the dewpoint temperature. The black sounding and indices correspond to the observed 1200 UTC sounding, while the red sounding and indices correspond to the 1800 UTC sounding at the closest gridpoint using the 1800 UTC GFS analysis. The severe weather parameters calculated with the sounding data are surface-based CAPE (SBCAPE), most unstable CAPE (MUCAPE), 0–3-km storm-relative helicity (SRH) and 0–6-km wind shear magnitude.

FIG. 5: GOES-16 10.35-μm Tb (K) at (a) 1630, (b) 1645, (c) 1700, (d) 1715, (e) 1730, (f) 1745, (g) 1800, (h) 1815, (i) 1830, (j) 1845, (k) 1900, (l) 1915, (m) 1930, (n) 1945, (o) 2000 and (p) 2015 UTC. The CTS cluster, PLS cluster, and other noteworthy features are indicated in the figures, as well as the occurrences of hail in each estimated time. All images were displaced to account for the parallax error.
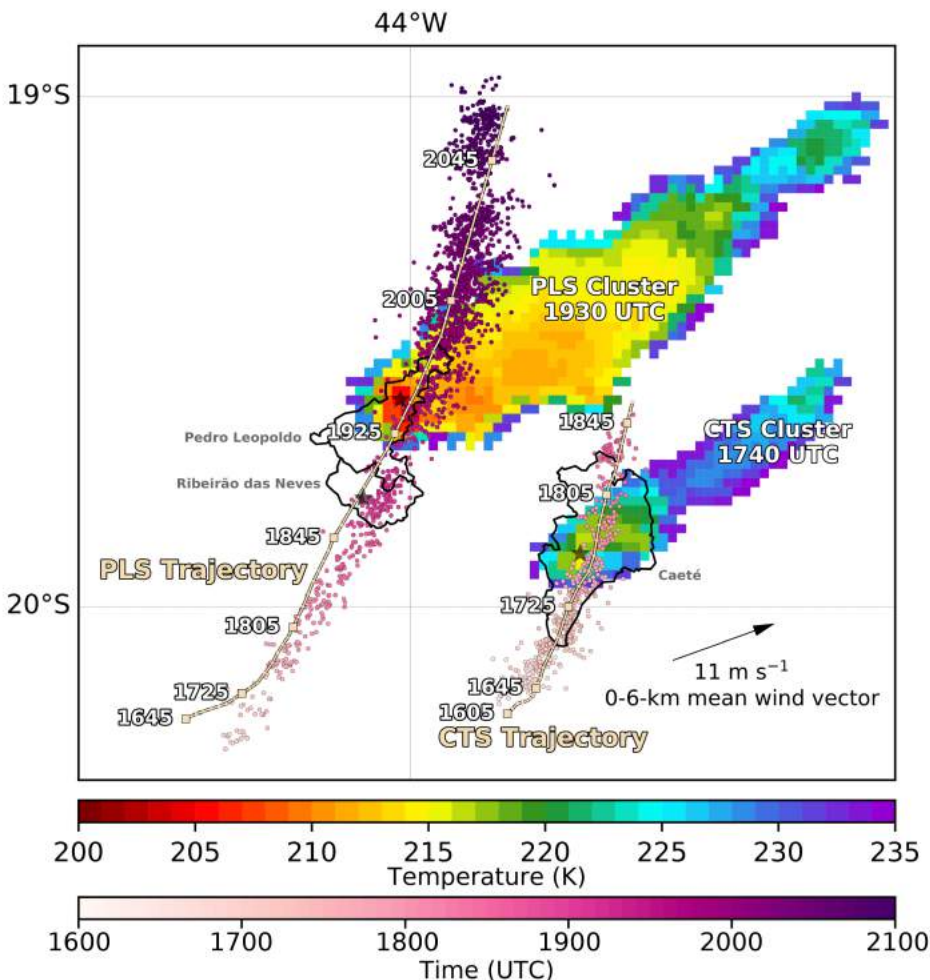
FIG. 6: GOES-16 10.35-μm Tb (K, shaded) in the CTS and PLS clusters (Tb<235 K) at 1740 and 1930 UTC, respectively, BrasilDAT total flashes (magenta dots, accumulated in 5-minute intervals according to the colorbar) and CTS and PLS trajectories derived from the 0.5° plan position indicator reflectivity centroids at each 5 minutes. The Caeté, Ribeirão das Neves and Pedro Leopoldo counties areas are delimited by thin black contours, and the stars mark the location of hail reports. The small squares along the storms trajectories indicate the time every 5 minutes, and the larger squares the time every 40 minutes (UTC, numbers at the left of the squares). The satellite-derived clusters were displaced to account for the parallax error.
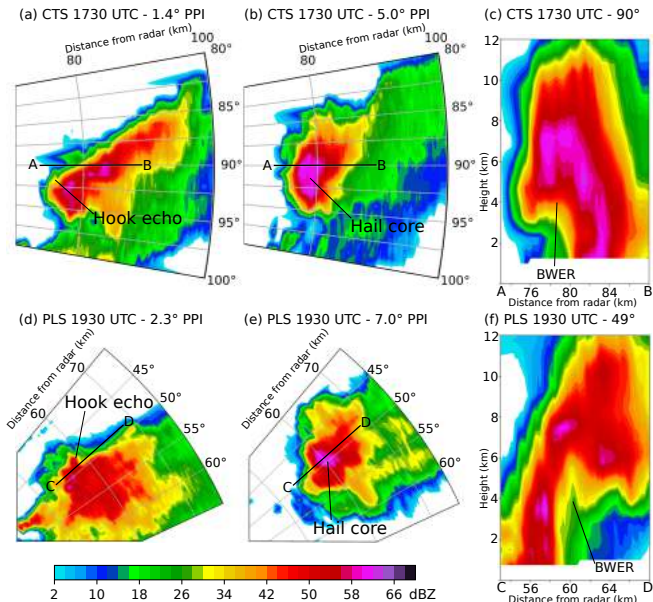
FIG. 7: Mateus Leme C-band radar reflectivity factor (dBZ) plots for CTS and PLS. CTS (a) 1.4° and (b) 5.0° PPIs and (c) vertical cross section along the 90° azimuth between A and B at 1730 UTC 29 November 2017. PLS (d) 2.3° and (e) 7.0° PPIs and (f) vertical cross section along the 49° azimuth between C and D at 1930 UTC 29 November 2017. Hook echoes, hail cores and BWERs are indicated.
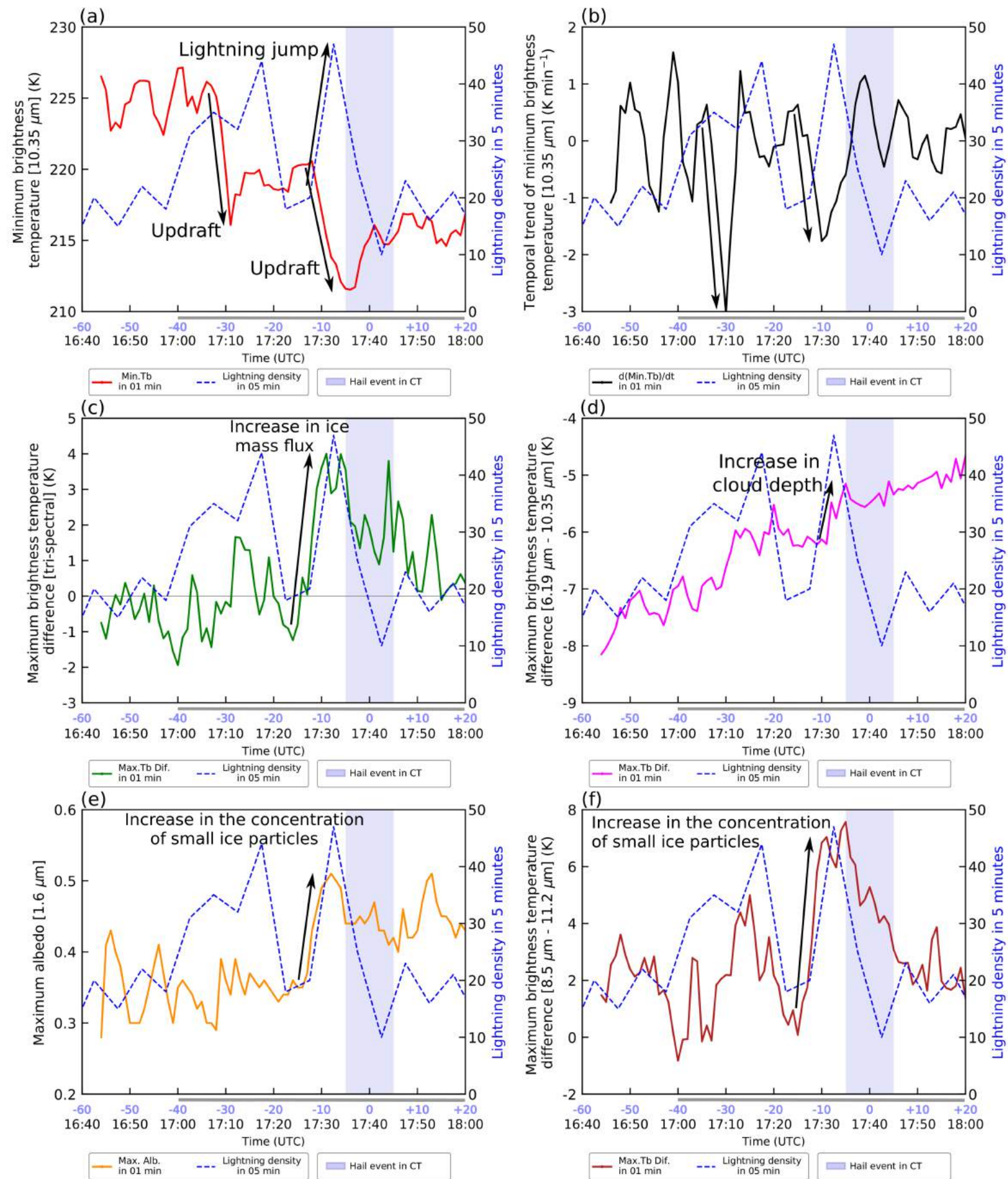
FIG. 8: Temporal variation of (a) minimum 10.35-µm Tb (K, red line), (b) temporal trend of 10.35-µm Tb (K min⁻¹, black line), (c) maximum tri-spectral difference (K, green line), (d) maximum difference between 6.19-µm Tb and 10.35-µm Tb (K, magenta line), (e) maximum 1.6-µm albedo (yellow line) and (f) maximum difference between 8.5-µm Tb and 11.2-µm Tb (K, dark red line) for the CTS cluster using GOES-16 data every 1 minute. The blue dashed line is the lightning strikes density (right vertical axis). The lightning density value is centered in the middle of the 5-minute period of accumulation. The shaded area is the estimated time of hailfall in Caeté. In the X axis, the colored labels are minutes relative to hailfall and black labels are time (UTC). The main physical processes associated with the trends are described. The grey line below the X axis indicates the periods when a hook echo was evident on radar in low elevation scans and/or a BWER was evident in cross sections.
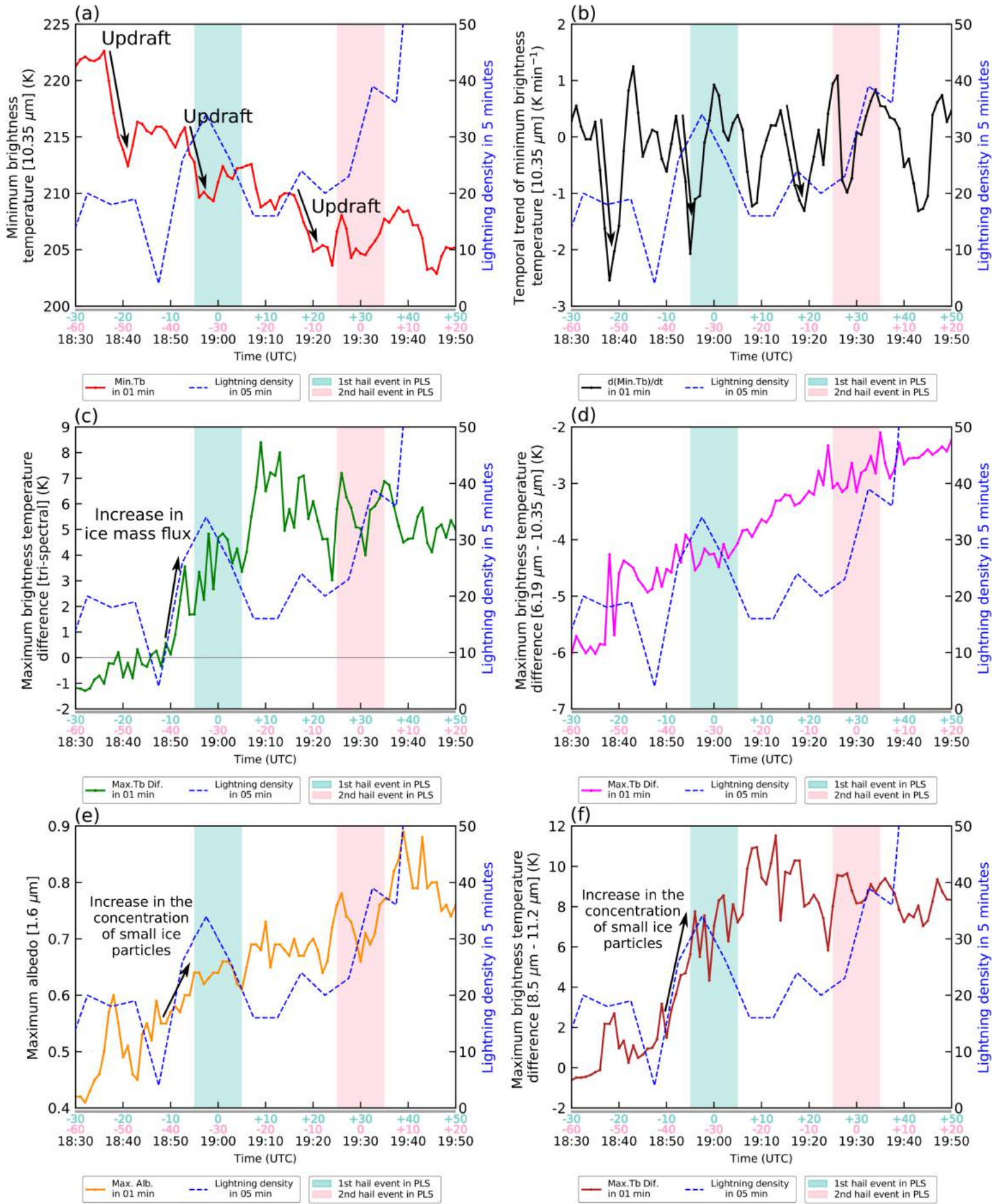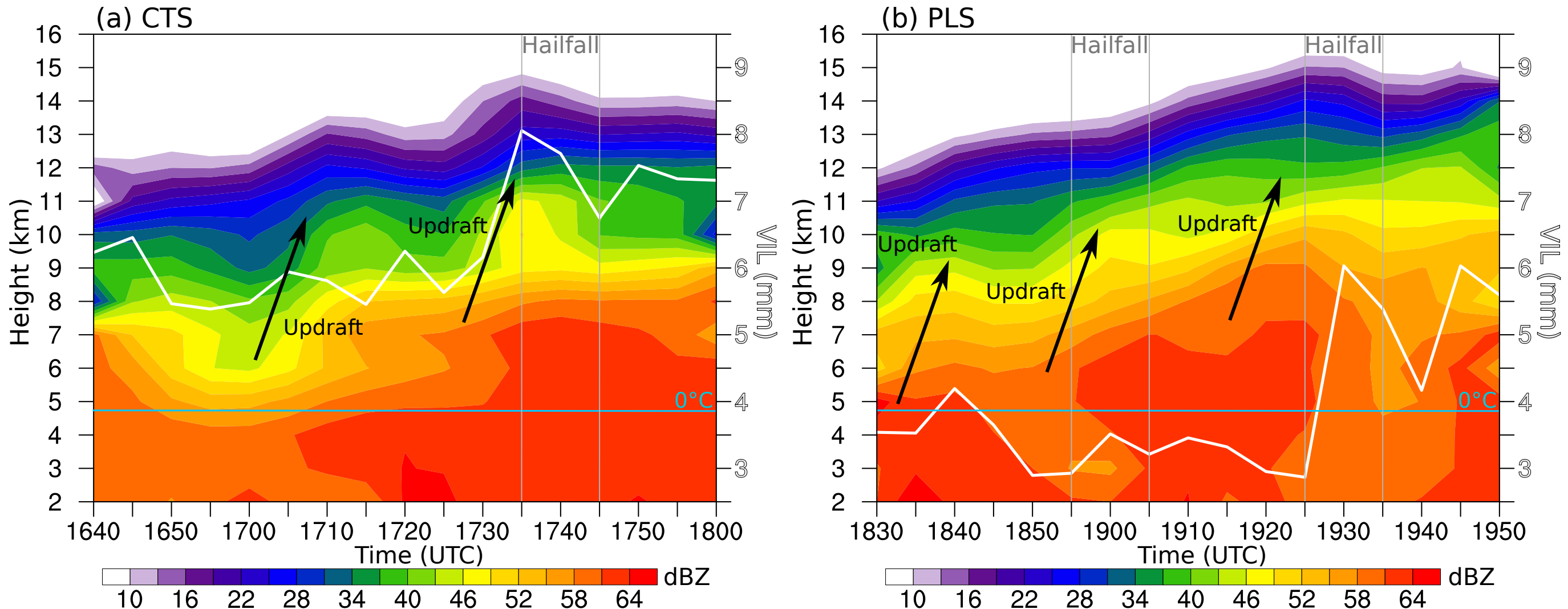
FIG. 9: Same as Figure 8, but for the PLS cluster. The leftmost shaded area is the Ribeirão das Neves 2-cm hail and wind event and the rightmost shaded area is the Pedro Leopoldo 5-cm hail event. In the X axis, the colored labels are minutes relative to hailfall (for each event according to the color) and black labels are time (UTC). The main physical processes associated with the trends are described. The grey line below the X axis indicates the periods when a hook echo was evident on radar in low elevation scans and/or a BWER was evident in cross sections.

FIG. 10: Temporal evolution of the vertical profile of reflectivity (dBZ, shaded) and average VIL (mm, white line) for the (a) CTS and (b) PLS clusters. The estimated times of hailfall are shown between grey lines. The light blue line indicates the 0°C isotherm height estimated using the 1200 UTC sounding (Fig. 4). The updrafts as inferred by the 10.35-μm Tb decreases (Fig. 8a for CTS and Fig. 9a for PLS) are indicated by black arrows.
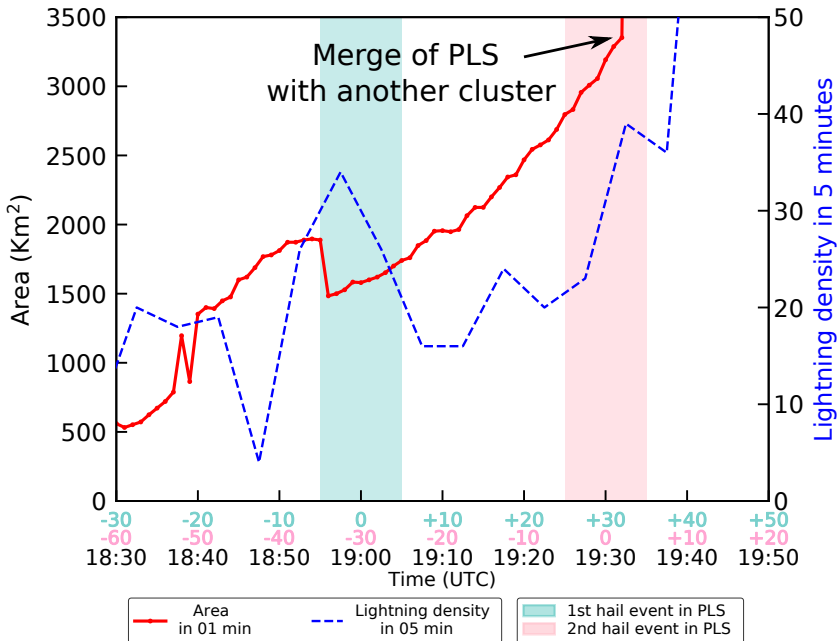
FIG. 11: Temporal variation of the PLS cluster area (km²). The leftmost shaded area is the Ribeirão das Neves 2-cm hail and wind event and the rightmost shaded area is the Pedro Leopoldo 5-cm hail event. In the X axis, the colored labels are minutes relative to hailfall (for each event according to the color) and black labels are time (UTC).
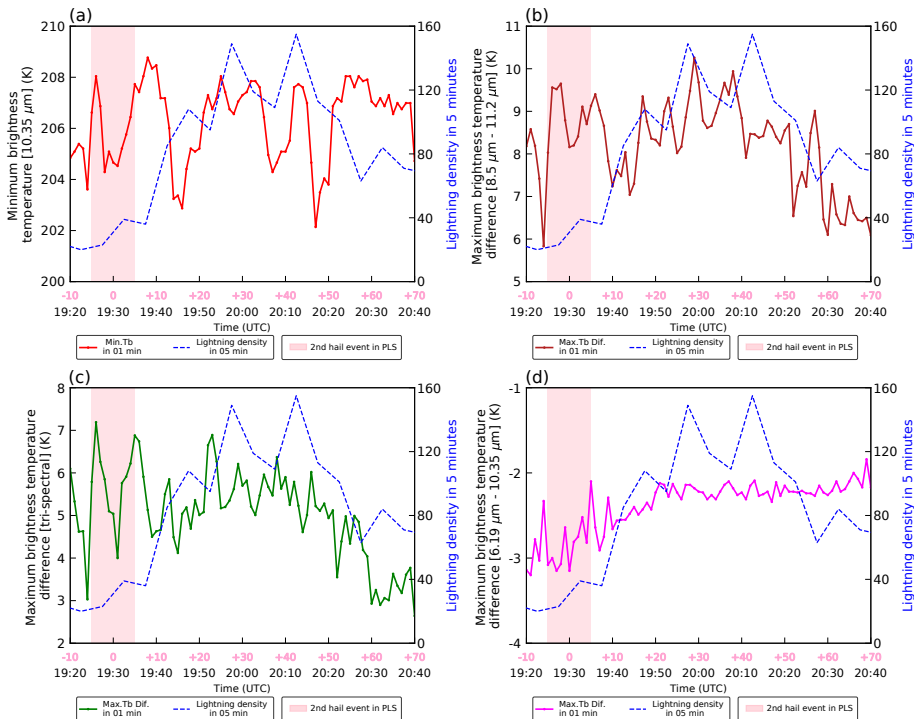
FIG. 12: Temporal variation of (a) minimum 10.35-μm Tb (K, red line), (b) maximum difference between 8.5-μm Tb and 11.2-μm Tb (K, dark red line), (c) maximum tri-spectral difference (K, green line) and (d) maximum difference between 6.19-μm Tb and 10.35-μm Tb (K, magenta line) for the PLS cluster mature stage using GOES-16 data every one minute. The blue dashed line is the lightning strikes density (right vertical axis). The lightning density value is centered in the middle of the 5-minute period of accumulation. The shaded area is the estimated time of hailfall in Pedro Leopoldo.
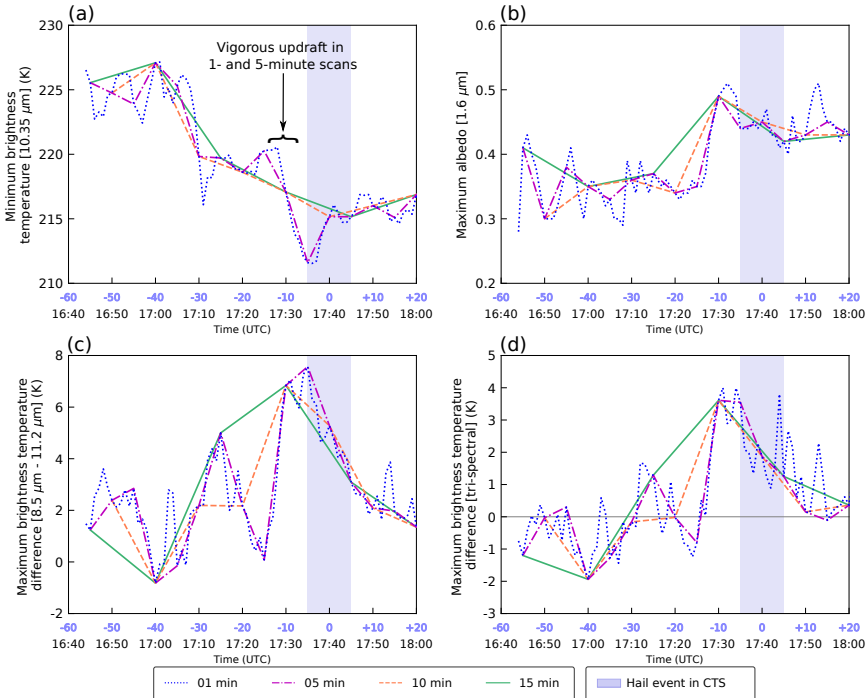
FIG. 13: Temporal variations of the satellite-derived parameters each 1 (blue dotted line), 5 (magenta dot-dashed line), 10 (orange dashed line) and 15 (green continuous line) minutes for the CTS cluster. (a) Minimum 10.35-μm Tb (K), (b) maximum 1.6-μm albedo, (c) maximum difference between 8.5-μm Tb and 11.2-μm Tb (K) and (d) maximum tri-spectral difference (K). The shaded area is the estimated time of hailfall in Caeté. In the X axis, the colored labels are minutes relative to hailfall and black labels are time (UTC). The occurrences of vigorous updrafts [8 K (15 min)$^{-1}$ decrease in 10.35-μm Tb] noticed in 1- and 5-minute scans but not in 10- and 15-minute scans are indicated.
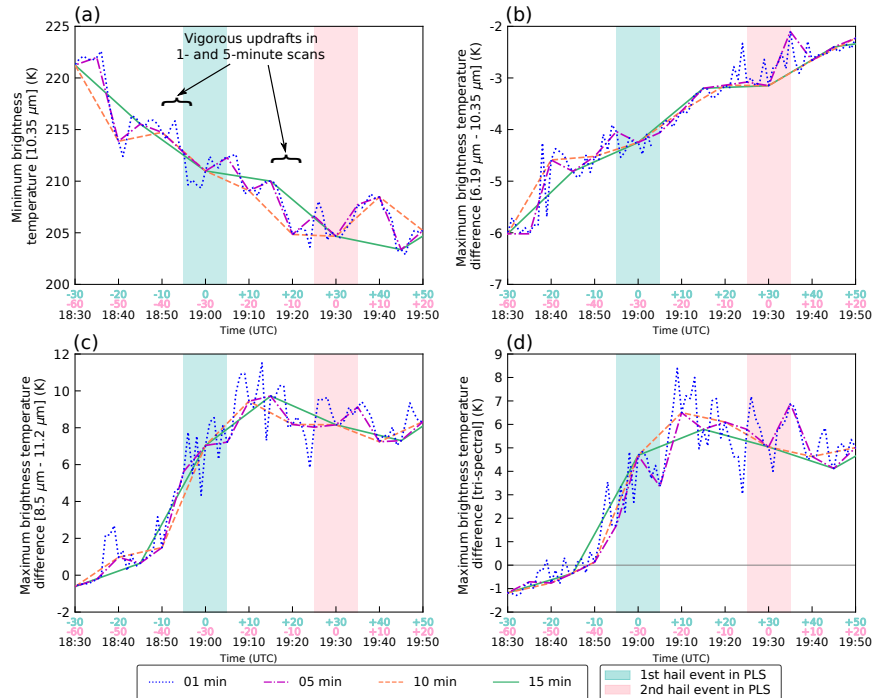
FIG. 14: Temporal variations of the satellite-derived parameters each 1 (blue dotted line), 5 (magenta dot-dashed line), 10 (orange dashed line) and 15 (green continuous line) minute for the PLS cluster. (a) Minimum 10.35-μm Tb (K), (b) maximum difference between 6.9-μm Tb and 10.35-μm Tb (K), (c) maximum difference between 8.5-μm Tb and 11.2-μm Tb (K) and (d) maximum tri-spectral difference (K). The leftmost shaded area is the Ribeirão das Neves 2-cm hail and wind event and the rightmost shaded area is the Pedro Leopoldo 5-cm hail event. In the X axis, the colored labels are minutes relative to hailfall (for each event according to the color) and black labels are time (UTC). The occurrences of vigorous updrafts [8 K (15 min)⁻¹ decrease in 10.35-μm Tb] noticed in 1- and 5-minute scans but not in 10- and 15-minute scans are indicated.